

# Refining the Identity and Role of Kv4 Channels in Mouse Substantia Nigra Dopaminergic Neurons

<https://doi.org/10.1523/ENEURO.0207-21.2021>

**Cite as:** eNeuro 2021; 10.1523/ENEURO.0207-21.2021

Received: 10 May 2021

Accepted: 17 May 2021

---

*This Early Release article has been peer-reviewed and accepted, but has not been through the composition and copyediting processes. The final version may differ slightly in style or formatting and will contain links to any extended data.*

**Alerts:** Sign up at [www.eneuro.org/alerts](http://www.eneuro.org/alerts) to receive customized email alerts when the fully formatted version of this article is published.

Copyright © 2021 Haddjeri-Hopkins et al.

This is an open-access article distributed under the terms of the Creative Commons Attribution 4.0 International license, which permits unrestricted use, distribution and reproduction in any medium provided that the original work is properly attributed.

# 1    **REFINING THE IDENTITY AND ROLE OF KV4 CHANNELS IN MOUSE** 2    **SUBSTANTIA NIGRA DOPAMINERGIC NEURONS**

3    **Abbreviated Title:** Kv4 channels in substantia nigra dopaminergic neurons

4    Alexis HADDJERI-HOPKINS<sup>1,\*</sup>, Mónica TAPIA<sup>1,\*</sup>, Jorge RAMIREZ-FRANCO<sup>1</sup>, Fabien TELL<sup>1,2</sup>,  
5    Béatrice MARQUEZE-POUEY<sup>1</sup>, Marianne AMALRIC<sup>3</sup> and Jean-Marc GOAILLARD<sup>1,2,§</sup>

6

7    <sup>1</sup> UMR\_S 1072, Aix Marseille University, INSERM, Faculté de Médecine Secteur Nord, 51 boulevard  
8    Pierre Dramard, 13015 Marseille, FRANCE

9    <sup>2</sup> Current address: Institut de Neurosciences de la Timone, UMR 7289, Aix-Marseille Université and  
10    Centre National de la Recherche Scientifique, Marseille, FRANCE.

11    <sup>3</sup> UMR7291, Aix Marseille University, CNRS, LNC, 3 place Victor Hugo, 13331 Marseille, FRANCE

12    \* These authors contributed equally to this work

13    § Corresponding author

14    **Corresponding author:** Jean-Marc GOAILLARD. [jean-marc.goillard@univ-amu.fr](mailto:jean-marc.goillard@univ-amu.fr)

15    **Author contributions:** M.A., F.T. and J-M.G. designed research. A.H-H., M.T., J.R.F., F.T. and B.M-P.  
16    performed research. A.H-H., M.T., J.R.F., F.T. and J-M.G. analyzed data. A.H-H., M.T., J.R.F., F.T.,  
17    M.A. and J-M.G. wrote the manuscript.

18    **Conflict of interest:** the authors declare no competing financial interests.

19    **Acknowledgements:** this work was supported by the European Research Council (Consolidator grant  
20    616827 *CanaloHmics* to J-M.G., supporting A.H-H. and M.T.), the Fondation de France (grant 00076344  
21    to J-M.G. and M.A., supporting A.H-H.), and the Agence Nationale pour la Recherche (ANR Logik ANR-  
22    17-CE16-0022, supporting J.R.F.). We thank O. Toutendji for technical assistance.

23

24 **ABSTRACT**

25 Substantia nigra pars compacta (SNc) dopaminergic (DA) neurons display a peculiar electrical  
26 phenotype characterized *in vitro* by a spontaneous tonic regular activity (pacemaking activity), a  
27 broad action potential and a biphasic post-inhibitory response. The transient A-type current ( $I_A$ ) is  
28 known to play a crucial role in this electrical phenotype, and so far this current was considered to  
29 be carried exclusively by Kv4.3 potassium channels. Using Kv4.3<sup>-/-</sup> transgenic mice, we  
30 demonstrate that the constitutive loss of this channel is associated with increased exploratory  
31 behavior and impaired motor learning at the behavioral level. Consistently it is also associated  
32 with a lack of compensatory changes in other ion currents at the cellular level. Using antigen  
33 retrieval immunohistochemistry, we then demonstrate that Kv4.2 potassium channels are also  
34 expressed in SNc DA neurons, even though their contribution to  $I_A$  appears significant only in a  
35 minority of neurons (~5-10%). Using correlative analysis on recorded electrophysiological  
36 parameters and multi-compartment modeling, we then demonstrate that, rather than its  
37 conductance level,  $I_A$  gating kinetics (inactivation time constant) appear as the main biophysical  
38 property defining post-inhibitory rebound delay and pacemaking frequency. Moreover, we show  
39 that the hyperpolarization-activated current ( $I_H$ ) has an opposing and complementary influence on  
40 the same firing features.

41

42

43

44 **SIGNIFICANCE STATEMENT**

45 Substantia nigra pars compacta (SNc) dopaminergic (DA) neurons are characterized by  
46 pacemaking activity, a broad action potential and biphasic post-inhibitory response. The A-type  
47 transient potassium current ( $I_A$ ) plays a central role in this electrical phenotype. While it was  
48 thought so far that Kv4.3 ion channels were fully responsible for  $I_A$ , using a Kv4.3<sup>-/-</sup> transgenic  
49 mouse and antigen retrieval immunohistochemistry we demonstrate that Kv4.2 channels are also  
50 expressed in SNc DA neurons, although their contribution is significant in a minority of neurons  
51 only. Using electrophysiological recordings and computational modeling, we then demonstrate  
52 that  $I_A$  gating kinetics and its functional complementarity with the hyperpolarization-activated  
53 current are major determinants of both pacemaking activity and post-inhibitory response in SNc  
54 DA neurons.

55

## 56 INTRODUCTION

57 While the expression of only two types of voltage-gated ion channels in the squid giant  
58 axon allowed Hodgkin and Huxley to dissect the biophysical processes underlying action  
59 potential (AP) genesis and conduction (Hodgkin and Huxley, 1952), most neuronal types express  
60 a multitude of ion channel subtypes underlying their electrical activity (Cembrowski et al., 2016;  
61 Fuzik et al., 2016; Tapia et al., 2018; Northcutt et al., 2019). In spontaneously active neurons, a  
62 variety of voltage- and calcium-gated ion channels are not only responsible for the AP, but also  
63 govern the subthreshold oscillations leading to AP firing, determine firing frequency and control  
64 its regularity (Atherton and Bevan, 2005; Swensen and Bean, 2005; Bean, 2007; Gantz et al.,  
65 2018). Substantia nigra pars compacta (SNc) dopaminergic (DA) neurons spontaneously generate  
66 a regular tonic pattern of activity, also known as "pacemaking" activity (Grace and Onn, 1989;  
67 Gantz et al., 2018). Over the past 40 years, many studies contributed to the identification of the  
68 specific ion channels involved in shaping pacemaking activity (Nedergaard and Greenfield, 1992;  
69 Liss et al., 2001; Seutin et al., 2001; Wolfart et al., 2001; Neuhoff et al., 2002; Liss et al., 2005;  
70 Chan et al., 2007; Puopolo et al., 2007; Guzman et al., 2009; Putzier et al., 2009; Ji et al., 2012;  
71 Gantz et al., 2018). In particular, several studies have suggested that the transient A-type  
72 potassium current ( $I_A$ ) plays an essential role in controlling pacemaking rate and post-inhibitory  
73 firing delay in these neurons (Liss et al., 2001; Putzier et al., 2008; Amendola et al., 2012; Tarfa  
74 et al., 2017). In addition, single-cell PCR, in situ hybridization and immunohistochemistry  
75 experiments suggested that the A-type current is carried exclusively by Kv4.3 ion channels  
76 (Serodio and Rudy, 1998; Liss et al., 2001; Ding et al., 2011; Dufour et al., 2014a; Tapia et al.,  
77 2018). Interestingly, several studies also suggested that the H-type current ( $I_H$ , carried by HCN  
78 channels) displays strong functional interactions with  $I_A$ , having for instance an opposite

79 influence on post-inhibitory rebound delay (Amendola et al., 2012; Tarfa et al., 2017). The gating  
80 properties of these two currents were also shown to be co-regulated in rat SNc DA neurons  
81 (Amendola et al., 2012).

82 In the current study, we used in particular electrophysiological recordings from wild-type  
83 (WT) and Kv4.3<sup>-/-</sup> mice to refine the identity and role of Kv4 channels in the firing of SNc DA  
84 neurons. Using this mouse model, we show that the constitutive loss of Kv4.3 is associated with  
85 increased exploratory activity and impaired motor learning. Consistently, it is also associated  
86 with a lack of compensatory changes in other ion currents at the cellular level. We then  
87 demonstrate that the Kv4.2 subunit is expressed in SNc DA neurons, although its functional  
88 contribution is minor in most SNc DA neurons. Finally, we also demonstrate that pacemaking  
89 frequency and post-inhibitory rebound delay are mainly determined by I<sub>A</sub> time constant of  
90 inactivation and I<sub>H</sub> amplitude.

91

## 92 MATERIAL AND METHODS

### 93 *Animals*

94 Female and male P15-P80 WT (n=68 animals) and Kv4.3<sup>-/-</sup> (n=40, Deltagen) mice from  
95 C57BL6/J genetic background were housed with free access to food and water in a temperature-  
96 controlled room (24°C) on a 12:12 h dark–light cycle (lights on at 07:00 h). All efforts were  
97 made to minimize the number of animals used and to maintain them in good general health,  
98 according to the European (Council Directive 86/609/EEC) and institutional guidelines for the  
99 care and use of laboratory animals (French National Research Council).

### 100 *Behavioral Experiments*

101 A group of female and male WT (n=11) and Kv4.3<sup>-/-</sup> (n=13) mice aged P56-P63 at the start of the  
102 behavioral testing were used to evaluate changes in motor function, using in particular locomotor  
103 activity chambers and the rotarod test.

### 104 Locomotor and exploratory activities

105 Actimetry was monitored in individual activity chambers (20 cm × 11.2 cm × 20.7 cm) housed  
106 within a sound-attenuating cubicle and under homogeneous illumination (Imetronic, Pessac,  
107 France). Each chamber was equipped with two pairs of infrared photobeams located 1.5 and  
108 7.5cm above the floor level of the chamber. The number of back-and-forth movements (animals  
109 breaking the lower photobeams) as well as the number of vertical movements (animals breaking  
110 the upper photobeams) were recorded in 5-min bins over 90 min. Numbers of back-and-forth  
111 movements (locomotion) and vertical movements (rearing) are shown as mean ± SEM for each

time bin over the whole period of recording time. Locomotion and rearing activities over the whole 90-min period were normalized and displayed as a mean percentage of control littermates.

#### Motor learning

Motor learning was evaluated on the accelerating rotarod (10cm diameter rod) test at a speed of 5 to 40 rotations per min (RPM) for 5 min. On the first day, mice were allowed to freely explore the non-rotating apparatus for 60s and subsequently trained to hold on the rotating rod (5 RPM) for at least two 60s trials, each trial being separated by a 10min break. Mice were allowed to recover for one hour before the first test. The testing phase consisted in 10 consecutive trials on the accelerating rod separated by 15-min breaks that allowed consolidation of performance. Results are shown as the average latency to fall off the rod (mean  $\pm$  SEM) at each trial. A *performance index* was calculated for each individual and consisted in the average latency of the last 3 trials divided by the average latency of the first 3 trials multiplied by 100 ( $\frac{\text{average latency } 8-10}{\text{average latency } 1-3} \times 100$ ).

#### ***Electrophysiology***

119 neurons from 39 WT mice and 109 neurons from 24 Kv4.3<sup>-/-</sup> mice were recorded (current-clamp and voltage-clamp).

#### Acute midbrain slice preparation

Acute slices were prepared from P15-P25 animals of either sex. Mice were anesthetized with isoflurane (CSP) in an oxygenated chamber (TEM SEGA) before decapitation. After decapitation the brain was immersed briefly in oxygenated ice-cold low-calcium aCSF containing the following (in mM): 125 NaCl, 25 NaHCO<sub>3</sub>, 2.5 KCl, 1.25 NaH<sub>2</sub>PO<sub>4</sub>, 0.5 CaCl<sub>2</sub>, 4 MgCl<sub>2</sub>, and



133 25 D-glucose, pH 7.4, oxygenated with 95% O<sub>2</sub>/5% CO<sub>2</sub> gas. The cortices were removed and  
 134 then coronal midbrain slices (250  $\mu$ m) were cut in ice-cold oxygenated low-calcium aCSF on a  
 135 vibratome (Leica VT1200S and vibrating microtome 7000smz, Camden Instruments, UK).  
 136 Following 20-30 min incubation in oxygenated low-calcium aCSF at 33°C, the acute slices were  
 137 then incubated for a minimum of 30 min in oxygenated aCSF (containing in mM: 125 NaCl, 25  
 138 NaHCO<sub>3</sub>, 2.5 KCl, 1.25 NaH<sub>2</sub>PO<sub>4</sub>, 2 CaCl<sub>2</sub>, 2 MgCl<sub>2</sub>, and 25 glucose, pH 7.4, oxygenated with  
 139 95% O<sub>2</sub>/5% CO<sub>2</sub> gas) at room temperature before electrophysiological recordings.

#### 140 Drugs

141 Kynurenate (2 mM, Sigma-Aldrich) and picrotoxin (100  $\mu$ M, Sigma-Aldrich) were used to block  
 142 excitatory and inhibitory synaptic activity, respectively. AmmTX3 (1  $\mu$ M, Alomone) was used to  
 143 block the transient potassium current (I<sub>A</sub>) carried by Kv4 channels. Drugs were bath applied via  
 144 continuous perfusion in aCSF.

#### 145 Electrophysiology recordings and analysis

146 All recordings (228 neurons from 63 mice) were performed on midbrain slices continuously  
 147 superfused with oxygenated aCSF at 30–32°C. Picrotoxin and kynurenate were systematically  
 148 added to the aCSF for all recordings to prevent contamination of the intrinsically generated  
 149 activity by glutamatergic and GABAergic spontaneous synaptic activity. Patch pipettes (1.9–2.7  
 150 MOhm) were pulled from borosilicate glass (GC150TF-10, Harvard Apparatus) on a DMZ-  
 151 Universal Puller (Zeitz Instruments) and filled with a patch solution containing the following (in  
 152 mM): 20 KCl, 10 HEPES, 0.5 EGTA, 2 MgCl<sub>2</sub>, 0.4 Na-GTP, 2 Na<sub>2</sub>-ATP, 4 Mg-ATP, 0.3 CaCl<sub>2</sub>,  
 153 SUPERase RNase inhibitor (0.1 U/ $\mu$ l) and 115 K-gluconate, pH 7.4, 290–300 mOsm. For  
 154 AmmTX3 experiments, patch pipettes (3.2-4.0 MOhm) were filled with a patch solution

155 containing the following (in mM): 20 KCl, 10 HEPES, 0.5 EGTA, 2 MgCl<sub>2</sub>, 2 Na-ATP, and 120  
156 K-gluconate, pH 7.4, 290–300 mOsm. Whole-cell recordings were made from SNc DA neurons  
157 visualized using infrared differential interference contrast videomicroscopy (QImaging Retiga  
158 camera; Olympus BX51WI microscope), and were identified based on their location, large soma  
159 size (>25µm), and electrophysiological profile (regular slow pacemaking activity, large spike  
160 half-width, large sag in response to hyperpolarizing current steps). For voltage-clamp  
161 experiments, only whole-cell recordings with an uncompensated series resistance <7 MOhm  
162 (compensated 85–90%) were included in the analysis. For current-clamp pharmacology  
163 experiments, higher series resistances were tolerated as long as the bridge compensation was  
164 properly adjusted to 100%. Liquid junction potential (-13.2 mV) and capacitive currents were  
165 compensated on-line. Recordings were acquired at 50kHz and were filtered with a low-pass filter  
166 (Bessel characteristic 2.8kHz cutoff). For current-clamp recordings, 1s hyperpolarizing current  
167 steps were injected to elicit a hyperpolarization-induced sag (due to I<sub>H</sub> activation).

#### 168 Current-clamp recordings and protocols

169 The spontaneous firing frequency was calculated from a minimum of 30 s of stable recording in  
170 cell-attached mode and from current-clamp recording (with no injected current) within the first 5  
171 min after obtaining the whole-cell configuration. The coefficient of variation of the interspike  
172 interval (CV<sub>ISI</sub>) was extracted from the same recording. Action potentials (APs) generated during  
173 this period of spontaneous activity were averaged and several parameters were extracted: AP  
174 threshold, AP amplitude, AP duration at half of its maximal height (AP half-width), AHP trough  
175 voltage, AHP latency. Hyperpolarizing current steps and depolarizing current steps were used to  
176 characterize the post-inhibitory rebound and the excitability properties. The gain start, gain end

177 and spike frequency adaptation (SFA) index used to define excitability were calculated as  
178 described before (Dufour et al., 2014b).

#### 179 Voltage-clamp recordings

180 The  $I_A$  current was elicited by a protocol consisting in a 500 ms prestep at -100 mV (to fully de-  
181 inactivate  $I_A$ ) followed by a 500 ms voltage step to -40 mV (to activate  $I_A$  without eliciting  
182 delayed rectifier potassium currents). The current generated by the same protocol using a prestep  
183 at -40mV (to fully inactivate  $I_A$ ) was subtracted to isolate  $I_A$ .  $I_A$  properties (peak amplitude and  
184 total charge) were measured after subtracting the baseline at -40mV. Total charge was calculated  
185 by integrating the current over the whole duration (500ms) of the voltage step. The peak of the  
186 current elicited at -40mV was then plotted against the voltage of each corresponding prestep, and  
187 was fitted with a Boltzmann function to obtain  $I_A$  half-inactivation voltage ( $V_{50 I_A}$ ) (see  
188 (Amendola et al., 2012)). The inactivation time constant ( $I_A$  tau) was extracted from a mono-  
189 exponential fit of the decay of the current. A two-step voltage-clamp protocol was used to  
190 determine the voltage-dependence of activation of  $I_H$  ( $V_{50 I_H}$ ) and obtain the maximum  $I_H$   
191 amplitude (see (Amendola et al., 2012) for details). For voltage-clamp recordings of delayed  
192 rectifier current ( $I_{KDR}$ ), tetrodotoxin (1  $\mu$ M, Alomone), nickel (200  $\mu$ M, Sigma-Aldrich) and  
193 cadmium (400  $\mu$ M, Sigma-Aldrich) were also added to the aCSF.  $I_{KDR}$  was elicited by using a  
194 protocol consisting in a prestep at -40mV (to fully inactivate  $I_A$ ) followed by incremental  
195 depolarizing voltage steps up to +40mV.

#### 196 Data acquisition

197 Data were acquired using an EPC 10 USB patch-clamp amplifier (HEKA) and the Patchmaster  
198 software acquisition interface (HEKA). Analysis was performed using FitMaster v2x73 (Heka).

199 ***Immunohistochemistry***

200 Adult (P21-P28) C57BL/6 WT mice (n=2) or Kv4.3<sup>-/-</sup> littermates (n=2) of either sex were  
 201 euthanized with ketamine-xylazine mix (100mg/Kg ketamine, 10mg/Kg xylazine), and  
 202 transcardially perfused with PBS and ice-cold 4% paraformaldehyde in PBS. Brains were  
 203 removed and post-fixed overnight (o/n) at 4°C in the same fixative solution. Coronal brain slices  
 204 of 50 µm were obtained using a vibratome (vibrating microtome 7000smz, Camden Instruments,  
 205 UK) and collected as floating sections. When indicated, antigen retrieval was performed by  
 206 incubating the slices in sodium citrate (10mM, Sigma-Aldrich) during 30 min at 80°C (Jiao et al.,  
 207 1999). Subsequently, slices were blocked for 1 h 30 min at room temperature (RT) in a solution  
 208 containing 0.3% Triton X-100 (SIGMA) and 5% Normal Goat Serum (NGS, Vector  
 209 Laboratories) in PBS. After blocking, sections were incubated with primary antibodies in a  
 210 solution containing 0.3% Triton X-100 and 1% NGS in PBS (o/n; 4°C). The following primary  
 211 antibodies were used in this study: Chicken anti-TH (1:1000; Abcam, ab76442,  
 212 RRID:AB\_1524535), Rabbit anti Kv4.3 (1:500, Alomone Labs, APC-017, RRID:AB\_2040178),  
 213 Mouse anti Kv4.2 (1:200, Neuromab, 75-361, clone L28/4, RRID:AB\_23155873). After three  
 214 washes (15 min/each) in PBS containing 0.3% Triton X-100, the floating sections were incubated  
 215 with the following secondary antibodies: Alexa 488-Goat anti-mouse (1:200, Jackson  
 216 ImmunoResearch), Alexa 488-Goat anti-rabbit (1:200, Jackson ImmunoResearch) and Alexa  
 217 594-Goat anti-chicken (1:200, Jackson ImmunoResearch) in a PBS solution containing 0.3%  
 218 Triton X-100 and 1% NGS for 2 h at RT. Finally, sections were washed three times  
 219 (15min/each), incubated with DAPI (1.5 µg/mL; Sigma-Aldrich) for 10 min, and mounted in  
 220 Vectashield (Vector Laboratories). Sections were stored at 4°C, and images were acquired on a  
 221 Zeiss LSM-780 confocal scanning microscope. All experiments involving WT and Kv4.3<sup>-/-</sup>

comparisons were performed in parallel applying the same acquisition settings to both genotypes. Images were processed and analyzed with ImageJ (NIH). Kv4.2-positive cells were visually identified in both genotypes on the basis of a perimembranous-like Kv4.2 staining and expressed as a percentage of the total number of TH+ cells. In order to compare the labeling pattern of Kv4.2 and Kv4.3, the line selection tool was used to trace 3µm-length lines perpendicular to the cell perimeter in individual optical sections. In each cell, 3 regions were analyzed, and 5 cells were used to calculate the average profile in each condition. Raw intensity values were collected, normalized (0-1 range) to the maximal value, and plotted as a function of distance (0 corresponding to Kv4 peak fluorescence signal, negative distances to extracellular space and positive distances to intracellular space; see **Figure 5B**). All the images shown are one single optical slice. For the sake of representation and to overcome differences regarding levels of TH expression in different DA neurons, different minimum and maximum display settings were applied in **Figure 5C** exclusively for the TH channel.

### Modeling

Simulations were performed using NEURON 7.5 software (Hines and Carnevale, 2001) as previously described (Moubarak et al., 2019). Realistic morphologies of 22 rat SNc DA neurons obtained previously were used to build multicompartment models (Moubarak et al., 2019). For each compartment, membrane voltage was obtained as the time integral of a first-order differential equation:

$$\frac{dV}{dt} = -\frac{1}{C_m} * \sum [g_i * (V_m - E_{rev})] - I_{axial}$$

where  $V_m$  is the membrane potential,  $C_m$  the membrane capacitance,  $g_i$  are ionic conductances and  $E_{rev}$  their respective reversal potentials. The axial flow of current ( $I_{axial}$ ) between adjacent

compartments is calculated by the NEURON simulation package (Hines and Carnevale, 2001). Cytoplasmic resistivity, specific membrane capacitance and specific membrane resistance were set to 150 Ohm.cm, 0.75  $\mu\text{F}/\text{cm}^2$ , and 100,000 Ohm.cm<sup>2</sup>, respectively, with  $E_{\text{rev}}$  for the leak conductance set at -50 mV. Six active conductances were included in the model: fast sodium ( $I_{\text{Na}}$ ), delayed rectifier potassium ( $I_{\text{KDR}}$ ), transient potassium ( $I_{\text{A}}$ ), L-type calcium ( $I_{\text{CaL}}$ ), hyperpolarization-activated ( $I_{\text{H}}$ ) and small conductance calcium-activated potassium ( $I_{\text{SK}}$ ) currents (Moubarak et al., 2019). Active conductances followed activation-inactivation Hodgkin-Huxley kinetics (**Table 2**). Parameters for  $I_{\text{A}}$ ,  $I_{\text{CaL}}$ ,  $I_{\text{SK}}$ ,  $I_{\text{Na}}$ ,  $I_{\text{KDR}}$  and  $I_{\text{H}}$  were based on our previous model and published values for SNc DA neurons (Gentet and Williams, 2007; Seutin and Engel, 2010; Amendola et al., 2012; Philippart et al., 2016; Moubarak et al., 2019). Intracellular calcium uptake was modeled as a simple decaying model according to Destexhe (Destexhe et al., 1993). Conductance values were set according to our own measurements or published values (see **Table 2**). Consistent with the literature (Kole and Stuart, 2008; Hu et al., 2009),  $g_{\text{Na}}$  and  $g_{\text{KDR}}$  were set to higher values in the axon initial segment (AIS) than in the rest of the neuron so that the action potential always initiated in the AIS. For sake of simplicity, activation and inactivation kinetics of  $I_{\text{A}}$  were voltage-independent but coupled to each other, such that activation rate was 50 times faster than inactivation rate. In addition the inactivation and activation  $V_{50}$ s were also coupled (50 mV shift). As  $I_{\text{A}}$  and  $I_{\text{H}}$  voltage-dependences have been shown to be positively correlated in rat SNc DA neurons (Amendola et al., 2012), both values were forced to co-vary in the model according to the equation  $V_{50}^{\text{inact. } I_{\text{A}}} = 0.814 \cdot (V_{50}^{\text{act. } I_{\text{H}}}) + 3.36$ .

Initializing potential was set at -70 mV and pacemaking frequency was let to stabilize (4 spikes) before further analysis. Each simulation run had a duration of 8000 ms with a dt of 0.02 ms.

266 Spatial discretization followed the “d\_lambda rule” (Hines and Carnevale, 2001). All dendritic  
267 compartments and the axon-start compartment contained all currents whereas AIS and axon only  
268 contained fast sodium ( $I_{Na}$ ) and delayed rectifier potassium ( $I_{KDR}$ ) currents. To measure post-  
269 inhibitory rebound delay, current injection was performed by inserting a virtual electrode in the  
270 soma. A 1s pulse of current was injected into the model. Negative current amplitude was adjusted  
271 to achieve a peak hyperpolarization around -120 mV in each neuron and condition. Firing  
272 frequency, rebound delay and action potential property analyses were computed online by  
273 handmade routines directly written in NEURON hoc language (Hines and Carnevale, 2001). This  
274 model is derived from a previous model available at model DB database under the number  
275 245427.

#### 276 *Statistics*

277 All statistical analyses were conducted under the R environment with appropriate packages. For  
278 behavioral experiments, normality was assessed by visual inspection of quantile-quantile (Q-Q)  
279 plots for the different scores per animal (ggpubr package). Nearly all the data points did not  
280 depart for normality estimated within a 95% coefficient interval. For electrophysiology  
281 experiments, normality was checked using the Shapiro-Wilk normality test (stat package).

#### 282 Behavior

283 To assess locomotor and exploratory behavior, number of horizontal (locomotion) and vertical  
284 (rearing) photobeam breaks was measured per 5-min bin over 90 min and compared between  
285 genotypes. As no significant difference was found between males and females in any of the  
286 behavioral tests, both sexes were pooled and analyzed as a single sample. Data are represented as  
287 line and scatter plots for the number of horizontal and vertical photobeam breaks per 5-min bin.



288 The number of total movements was then normalized to the level of WT spontaneous  
 289 locomotion. To assess the locomotor phenotype of Kv4.3<sup>-/-</sup> mice, two-way repeated measures  
 290 ANOVA tests with groups (WT/Kv4.3<sup>-/-</sup>) as the independent between-factor and time as the  
 291 within-factor (training sessions or time-bins for locomotion) were performed (stat package).  
 292 When the ANOVA was significant, multiple comparisons (false-discovery rate (fdr) adjustment,  
 293 multcomp and emmeans packages) were used to evaluate differences between groups at different  
 294 time points (Benjamini and Hochberg, 1995). P-values <0.05 were considered as statistically  
 295 significant for all analyses. For motor learning, the average latency to fall off the accelerating  
 296 rotarod was measured for each trial. Statistical difference in motor learning was assessed by  
 297 comparing the *performance index*. Data are represented as line and scatter plots for the average  
 298 latency to fall off the rod. Data are represented as mean ± SEM.

#### 299 Electrophysiology and immunohistochemistry

300 The univariate statistical analysis of electrophysiological data, performed according to the  
 301 distribution properties of the data using a Shapiro-Wilk normality test, included paired t-test or  
 302 Wilcoxon signed rank test; t-test or Mann-Whitney Wilcoxon test with  $p < 0.05$  considered to be  
 303 statistically significant (stat package). In most figures, data are represented as scatter plots or box  
 304 and whisker plots, with all individual points appearing on the graphs and dotted lines indicating  
 305 the distribution of data (violin plots). For pharmacological experiments, data are represented as  
 306 mean ± SEM (scatter or bar plots). Correlation, linear regression and multiple linear regression  
 307 analysis (**Figure 1, 9**) were performed in R. For every pair of variables, correlation parameters,  
 308 rho (Spearman correlation factor) or r (Pearson correlation factor), were selected after performing  
 309 a Shapiro-Wilk normality test on the linear regression residuals and p values were corrected for  
 310 multiple comparisons by an fdr adjustment (stat package). For multiple linear regression,



variables (extracellular ISI, rebound delay,  $I_A$  tau,  $I_H$  amplitude and  $I_A$  amplitude) were first log transformed, and then dependent variables were standardized (subtracting the mean and dividing by the SD). A selection of the best subsets of dependent variables for each model size (1 to 4 for the model and 1 to 5 for real data) was first performed (leaps package) according to several criteria (adjusted  $R^2$ , AIC, BIC). The best model was then selected by comparing the prediction error of each model after performing a repeated (20 times) 10-fold cross-validation on test data (caret package). The best linear model, corresponding to the minimum cross-validation error (i.e. a model with the best predictive power) was then obtained. Multicollinearity was assessed by computing a score called the variance inflation factor (VIF package) and VIF was  $< 1.5$  for all variables retained in the different models. For the immunohistochemistry experiments, a Fisher exact test was used to compare the proportions of Kv4.2-positive cells among TH-positive cells in WT and Kv4.3<sup>-/-</sup> mice. Figures were prepared using R, SigmaPlot 11.0, GraphPad Prism 6 and Adobe Illustrator CS5/CS6.

324

## 325 **RESULTS**

### 326 *Motor learning impairment of the Kv4.3<sup>-/-</sup> transgenic mice*

In order to define the precise contribution of Kv4.3 channels to SNc DA neuron electrophysiological phenotype, we used Kv4.3 constitutive KO mice (Niwa et al., 2008; Carrasquillo et al., 2012; Granados-Fuentes et al., 2012). These mice have been used previously to study Kv4.3 function in cardiac ventricles (Niwa et al., 2008), in neurons of the suprachiasmatic nucleus (Granados-Fuentes et al., 2012) and in neocortical pyramidal neurons (Carrasquillo et al., 2012). No major defect in cardiac function or circadian locomotor behavior

333 was reported in these studies. As Kv4.3 is also strongly expressed in the SNc and in the ventral  
 334 tegmental area (VTA) (Serodio and Rudy, 1998), we first sought to determine whether Kv4.3  
 335 loss could affect SNc or VTA-related behaviors, such as locomotion and motor learning (**Figure**  
 336 **1**). As illustrated in **Figure 1A**, horizontal locomotor activity assessed in photocell activity  
 337 chambers was similar between Kv4.3<sup>-/-</sup> mice and their WT littermates ( $F_{1,21}=0.31$ ,  $p=0.58$ ,  
 338 between factor effect), both strains displaying a significant decrease of locomotion over time  
 339 ( $F_{17,357}=20.5$ ,  $p=2\cdot 10^{-16}$ , within factor effect). The exploratory behavior was higher in Kv4.3<sup>-/-</sup>  
 340 mice than WT littermates in particular during the first part of the session (**Figure 1A**), although  
 341 the overall exploratory activity was not significantly different between the two strains ( $F_{1,21}=1.42$ ,  
 342  $p=0.25$ , between factor effect). Again, both strains displayed a strong run-down of activity over  
 343 the whole 90-min testing time as a function of habituation to the locomotor activity chambers  
 344 ( $F_{17,357}=13.97$ ,  $p=2\cdot 10^{-16}$ , within factor effect). Consistent with the increased exploratory activity  
 345 at the start of the session for the Kv4.3<sup>-/-</sup> mice, the two-way repeated measures ANOVA revealed  
 346 a significant interaction between strains and time ( $F_{17,357}=1.87$ ,  $p=0.019$ ). Motor learning abilities  
 347 were then assessed using the rotarod test for ten consecutive trials (**Figure 1B**). While WT mice  
 348 improved their performance across trials, as shown by the increase in the latency-to-fall, Kv4.3<sup>-/-</sup>  
 349 mice were not able to adjust their performance over time. While the latency averaged over trials  
 350 was not different between the two strains ( $F_{1,22}=1.26$ ,  $p=0.28$ , between factor effect, two-way  
 351 repeated measures ANOVA), performance changed significantly across trials ( $F_{9, 198}=4.5$ ,  
 352  $p=2\cdot 10^{-5}$ , within factor effect), especially for WT mice. Consistent with the differences in latency  
 353 for the late trials (**Figure 1B**), the difference in learning between the two strains was revealed by  
 354 the strains\*trials interaction statistics ( $F_{9,198}=2.95$ ,  $p=0.0026$ ) and significant differences in fall-  
 355 off latencies of Kv4.3<sup>-/-</sup> and WT mice was found for the late trials (7 to 9, **Figure 1B**). In order to  
 356 better quantify the difference in learning between strains, we then calculated a performance index

357 based on the difference in latency for the first 3 trials against the last 3 trials. Consistent with the  
 358 ANOVA results, the performance index in this motor learning task was significantly lower for  
 359 the Kv4.3<sup>-/-</sup> mice (WT,  $176.9 \pm 21.4$ , n=11 vs Kv4.3<sup>-/-</sup>,  $111.2 \pm 8.3$ , n=13, p=0.006, unpaired t-  
 360 test, **Figure 1B**).

### 361 *Changes in electrophysiological phenotype of Kv4.3<sup>-/-</sup> SNc DA neurons*

362 Following the approach already used in a previous study (Dufour et al., 2014b), we then  
 363 performed an exhaustive current-clamp characterization of the firing properties of SNc DA  
 364 neurons to determine changes in phenotype associated with Kv4.3 deletion (**Table 1**). Passive  
 365 properties, spontaneous activity, post-inhibitory rebound, action potential shape and excitability  
 366 were assessed by measuring 16 different electrophysiological parameters in 75-101 WT and 66-  
 367 77 Kv4.3<sup>-/-</sup> neurons. The first obvious electrophysiological change observed was that spontaneous  
 368 activity (extracellularly recorded in cell-attached mode) was dramatically modified in Kv4.3<sup>-/-</sup>  
 369 SNc DA neurons (**Figure 2A, B**). Spontaneous firing rate was increased by ~2-fold in Kv4.3<sup>-/-</sup>  
 370 mice, as demonstrated by the significant decrease in interspike interval (ISI, **Figure 2A, B; Table**  
 371 **1**). Pacemaking regularity, measured by the coefficient of variation of the ISI (CV<sub>ISI</sub>) was also  
 372 significantly different in Kv4.3<sup>-/-</sup> mice, although CV<sub>ISI</sub> values were very low (<20%) in both WT  
 373 and Kv4.3<sup>-/-</sup> mice, indicating a highly regular tonic activity. Post-inhibitory rebound delay was  
 374 also dramatically decreased in Kv4.3<sup>-/-</sup> mice (**Figure 2C, D; Table 1**). However, the I<sub>H</sub>-mediated  
 375 voltage sag observed during prolonged hyperpolarization was not modified (**Figure 2C, D; Table**  
 376 **1**). Interestingly, most action potential parameters were unchanged in Kv4.3<sup>-/-</sup> mice, except for  
 377 action potential half-width, which was slightly larger (**Figure 3A; Table 1**). We also analyzed  
 378 neuronal excitability by measuring the responses of the neurons to increasing depolarizing  
 379 current steps (**Figure 3B**). Excitability was slightly increased in the DA neurons of Kv4.3<sup>-/-</sup> mice,

380 although this change only affected the initial response of neurons (gain start) to current injection  
 381 (**Figure 3B**; **Table 1**). Consistently, the frequency of the response of Kv4.3<sup>-/-</sup> neurons to a 100pA  
 382 step was also found to be significantly higher (**Figure 3B**, **Table 1**).

### 383 *Voltage-clamp characterization of I<sub>A</sub> in Kv4.3<sup>-/-</sup> SNc DA neurons*

384 We then directly investigated changes in the properties of I<sub>A</sub> by performing voltage-clamp  
 385 recordings in WT and Kv4.3<sup>-/-</sup> SNc DA neurons (**Figure 4**). A dramatic decrease in I<sub>A</sub> amplitude  
 386 was observed in Kv4.3<sup>-/-</sup> mice (**Figure 4A, B**; **Table 1**). However, a small transient residual  
 387 current with I<sub>A</sub>-like properties (voltage-dependent inactivation) was still present in all Kv4.3<sup>-/-</sup>  
 388 recordings (**Figure 4A**). Most interestingly, this residual current was completely blocked by the  
 389 Kv4-specific toxin AmmTX3 (n=4, no measurable residual current after toxin application;  
 390 **Figure 4A**), suggesting that a Kv4 subunit other than Kv4.3 is expressed at a low level in Kv4.3<sup>-/-</sup>  
 391 SNc DA neurons. We then measured its time constant of inactivation (I<sub>A</sub> tau) and calculated the  
 392 overall charge carried by the current (**Figure 4C-E**). Both parameters were strongly decreased in  
 393 Kv4.3<sup>-/-</sup> SNc DA neurons (**Figure 4C, D**; **Table 1**), although a minority of cells (n=5/42)  
 394 displayed values similar to the WT measurements for both of these parameters. Plotting I<sub>A</sub> charge  
 395 versus I<sub>A</sub> tau revealed the clear separation of values between the Kv4.3<sup>-/-</sup> and WT measurements,  
 396 except for the 5 cells identified before (**Figure 4E**). Based on these voltage-clamp data, it appears  
 397 that, although the Kv4.3 subunit by far predominates in WT SNc DA neurons, another Kv4  
 398 subunit is also expressed, at least in the Kv4.3<sup>-/-</sup> neurons. Although in most cases, the expression  
 399 level of this unidentified subunit is too low to compensate for the loss of Kv4.3, it generates an  
 400 A-type current that provides a minority of Kv4.3<sup>-/-</sup> SNc DA neurons (5/42=12%) with a “wild-  
 401 type” voltage-clamp phenotype.

402 *Using antigen retrieval to reveal the expression of Kv4.2 channels by SNc DA neurons*

403 Several studies have investigated the expression of A-type Kv channels in SNc DA neurons,  
 404 using in situ hybridization (Serodio et al., 1996; Serodio and Rudy, 1998), single-cell quantitative  
 405 PCR (Liss et al., 2001; Ding et al., 2011; Tapia et al., 2018) and immunohistochemistry (Liss et  
 406 al., 2001; Dufour et al., 2014a). A high level of expression for Kv4.3 (Liss et al., 2001; Dufour et  
 407 al., 2014a; Tapia et al., 2018) and the absence of Kv4.1 (Serodio and Rudy, 1998; Liss et al.,  
 408 2001; Ding et al., 2011) were consistently reported, while the presence of Kv4.2 is still debated.  
 409 In particular, while Kv4.2 mRNA has been detected in several studies (Ding et al., 2011; Tapia et  
 410 al., 2018), the protein was not detected by classical immunohistochemistry (Liss et al., 2001;  
 411 Dufour et al., 2014a). Interestingly, it has been shown that, depending on the brain region and the  
 412 subcellular location of the ion channel of interest, an antigen retrieval (AR) procedure may be  
 413 required to uncover potassium channel antigen epitopes before performing immunolabeling  
 414 (Lorincz and Nusser, 2008). We first confirmed that Kv4.3 was strongly expressed in SNc DA  
 415 neurons in WT mice, with the expected membrane profile of immunostaining, and that it was  
 416 absent from Kv4.3<sup>-/-</sup> SNc DA neurons (**Figure 5A**). We then performed Kv4.2 immunolabeling  
 417 with or without AR on the neocortex and the CA1 region of the hippocampus where this ion  
 418 channel is highly expressed (Serodio and Rudy, 1998). As can be seen in **Figure 5-1**, Kv4.2  
 419 immunostaining was greatly improved by AR, revealing a strong perisomatic and dendritic  
 420 staining of pyramidal cells in both regions. Therefore we implemented AR before performing  
 421 Kv4.2 immunostaining on WT midbrain slices (**Figure 5B**). Similar to what we observed in the  
 422 hippocampus and in the cortex, Kv4.2 immunostaining in the SNc was greatly improved by AR,  
 423 although only a minority of DA neurons (TH-positive) displayed a clear perisomatic Kv4.2 signal  
 424 compatible with membrane expression of the channel. In fact, the AR Kv4.2 staining profile of

Kv4.2-positive cells was very similar to the membrane staining profile observed for Kv4.3 (Figure 5B). This distinctive staining profile was then used to quantify the percentage of Kv4.2-positive SNc DA neurons in both WT and Kv4.3<sup>-/-</sup> mice (Figure 5C, D). The percentage of Kv4.2-positive cells was not significantly different between WT and Kv4.3<sup>-/-</sup> mice (WT 20/423=4.7% vs Kv4.3<sup>-/-</sup> 19/382=5%, p=1, Fisher exact test, Figure 5D), suggesting that Kv4.2 pattern of expression is not modified by the loss of Kv4.3. This percentage is not statistically different from the percentage of Kv4.3<sup>-/-</sup> SNc DA neurons presenting an atypically large and slow I<sub>A</sub> reported in Figure 4C-E (5/42=11.9% vs 19/382=4.6%, p=0.077, Fisher exact test). Moreover, the percentage of Kv4.2-positive DA neurons was very similar in the medial and lateral SNc of both WT (SNc medial 11/227=4.8% vs SNc lateral 9/196=4.6%, p=1, Fisher exact test) and Kv4.3<sup>-/-</sup> mice (SNc medial 13/218=6% vs SNc lateral 6/164=3.7%, p=0.35, Fisher exact test).

#### ***Lack of compensation in the face of Kv4.3 loss***

Genetic deletion of Kv4.2 channels in cortical pyramidal neurons is associated with compensatory modifications in a delayed rectifier-like (I<sub>KDR</sub>-like) potassium current (Nerbonne et al., 2008). Moreover, I<sub>H</sub> and I<sub>A</sub> have complementary influences on post-inhibitory firing in SNc DA neurons (Amendola et al., 2012; Tarfa et al., 2017). In order to reveal putative homeostatic compensations of Kv4.3 deletion in SNc DA neurons, we first performed a series of current-clamp recordings on a subset of neurons (n=18 for WT, n=32 for Kv4.3<sup>-/-</sup>) to compare the effect of acutely blocking Kv4 channels using the scorpion toxin AmmTX3 (Vacher et al., 2002) to the changes observed in the Kv4.3<sup>-/-</sup> mouse. Consistent with previous reports (Amendola et al., 2012; Tarfa et al., 2017), AmmTX3 strongly increased pacemaking frequency and dramatically reduced

447 post-inhibitory rebound delay (**Figure 6**). Most interestingly though, the magnitude of the effects  
 448 of the toxin was very similar to that observed in the Kv4.3<sup>-/-</sup> neurons: firing frequency was  
 449 increased by ~68% in both conditions (**Figure 6B**), while rebound delay was decreased by 87%  
 450 after AmmTX3 and by 82% in Kv4.3<sup>-/-</sup> mice (**Figure 6D**). Consistent with the data presented  
 451 earlier, these results strongly suggest that the Kv4-mediated A-type current is virtually  
 452 completely abolished in Kv4.3<sup>-/-</sup> SNc DA neurons and that its loss is not compensated by changes  
 453 in other Kv channels (and associated currents).

454 We then used voltage-clamp recordings to directly assess whether a decrease in  $I_A$  could be  
 455 compensated by a parallel decrease in  $I_H$  or a compensatory increase in  $I_{KDR}$  (Nerbonne et al.,  
 456 2008) (**Figure 7**). Unlike what has been described in cortical neurons following Kv4.2 deletion,  
 457  $I_{KDR}$  was not modified in Kv4.3<sup>-/-</sup> SNc DA neurons (**Figure 7A**).  $I_H$  was found to be slightly  
 458 larger in Kv4.3<sup>-/-</sup> SNc DA neurons (**Figure 7B**, **Table 1**), but its voltage sensitivity was  
 459 unchanged. Altogether, the voltage-clamp recordings of  $I_A$ ,  $I_{KDR}$  and  $I_H$  and the AR Kv4.2  
 460 immunostaining suggest that Kv4.3 loss is not compensated by changes in expression and/or  
 461 function of functionally-overlapping channels. These data provide a biophysical explanation for  
 462 the observation made earlier that the acute blockade of Kv4 channels produces an  
 463 electrophysiological phenotype qualitatively and quantitatively virtually identical to the Kv4.3  
 464 genetic deletion (**Figure 6**).

465 ***Bridging the gap between biophysical changes in  $I_A$  and  $I_H$  and variation in***  
 466 ***electrophysiological phenotype***

467 We then decided to investigate whether the cell-to-cell variations in  $I_A$  biophysical properties in  
 468 WT and Kv4.3<sup>-/-</sup> SNc DA neurons were predictive of variations in electrophysiological



phenotype (**Figure 8**). We first looked at potential correlations between firing parameters. As already presented in **Figure 2**, the most significant alterations in firing observed in Kv4.3<sup>-/-</sup> SNc DA neurons are a strong increase in spontaneous firing frequency (strong decrease in the extracellularly-measured ISI) and a strong decrease in post-inhibitory rebound delay. We found that extracellular ISI and rebound delay (log transformed) were strongly positively correlated with each other in both WT and Kv4.3<sup>-/-</sup> neurons (**Figure 8B**), although the slope of this relationship seemed slightly different between the two genotypes. We therefore tried to determine whether specific I<sub>A</sub> biophysical properties were better predictors of these variations in ISI or rebound delay (**Figure 8C**). We also analyzed the relationship between I<sub>H</sub> properties and ISI or rebound delay. Out of the 5 biophysical parameters analyzed (I<sub>A</sub> tau, I<sub>H</sub> amplitude, I<sub>A</sub> amplitude, I<sub>A</sub> inactivation V<sub>50</sub>, I<sub>H</sub> activation V<sub>50</sub>), only two parameters were significantly correlated with ISI or rebound delay: I<sub>A</sub> tau and I<sub>H</sub> amplitude (log transformed) were positively and negatively correlated, respectively, with both ISI and rebound delay in both WT and Kv4.3<sup>-/-</sup> neurons (**Figure 8C**). Surprisingly, neither I<sub>A</sub> amplitude (measured at -40mV) nor its voltage-dependence (inactivation V<sub>50</sub>) were predictive of variations in ISI or rebound delay (**Figure 8C**). I<sub>H</sub> activation V<sub>50</sub> was also unable to predict variations in these firing parameters (data not shown). In addition, reminiscent of the observation made in rat neurons (Amendola et al., 2012), I<sub>H</sub> activation and I<sub>A</sub> inactivation V<sub>50</sub>s were found to be positively correlated (**Figure 8D**). I<sub>A</sub> tau and I<sub>H</sub> amplitude were also found to be negatively correlated (**Figure 8D**). Based on these observations, we then tested whether combining several of these 5 biophysical parameters could improve the prediction of ISI or rebound delay using multiple linear regression (**Figure 8E**). We first standardized these parameters (subtracting the mean and dividing by the SD), and then looked for the best subset of variables predictive of ISI or rebound delay. While ISI was best predicted by a multiple linear regression involving only I<sub>A</sub> tau and I<sub>H</sub> amplitude, rebound delay was better predicted when I<sub>A</sub>



tau,  $I_H$  amplitude and  $I_A$  inactivation  $V_{50}$  were included in the linear regression (**Figure 8E**). Rebound delay prediction was much more accurate than ISI prediction ( $r^2=0.771$  compared to  $r^2=0.421$ ). Based on the scaling factors given by the multiple linear regression, it is important to note that both ISI and rebound delay in real neurons seem to be most sensitive to variations in  $I_A$  tau.

#### ***Influence of $I_A$ biophysical properties on SNc DA neuron firing***

Many conductances other than  $I_A$  and  $I_H$  may vary in expression level and biophysical properties from neuron to neuron, potentially compensating or enhancing the effect of variations in the properties of these two currents on firing (Gentet and Williams, 2007; Puopolo et al., 2007; Seutin and Engel, 2010; Amendola et al., 2012; Philippart et al., 2016; Moubarak et al., 2019). In order to isolate the influence of specific biophysical properties of  $I_A$  and  $I_H$  on SNc DA neuron activity, we used a realistic multi-compartment Hodgkin-Huxley model of rat SNc DA neurons (Moubarak et al., 2019). Based on measurements obtained by different groups (Liss et al., 2001; Gentet and Williams, 2007; Amendola et al., 2012; Tarfa et al., 2017), each of the biophysical properties of  $I_A$  (maximal conductance  $g_A$ , voltage-dependence  $I_A$   $V_{50}$ , inactivation rate  $I_A$  tau) and  $I_H$  maximal conductance ( $g_H$ ) were varied over a 10-fold range (20mV range for the voltage-dependence) using 5 equi-distributed values (**Figure 9A**).  $I_A$  and  $I_H$  voltage-dependences were forced to co-vary in the model, based on our previous observations (Amendola et al., 2012). Using a sample of 22 realistic models and 5 independently-varying values for each biophysical property, a database of 13750 models ( $22 \times 5^4$ ) was generated (**Figure 9**). The average interspike interval (ISI) during spontaneous activity and the post-inhibitory firing delay in response to a hyperpolarizing pulse (rebound delay) were measured for each model and their average values were calculated for each combination of values of the 4 biophysical parameters ( $n=625$ ).

516 Dimensional stacking (Taylor et al., 2006) was then used to represent the influence of the 4  
 517 biophysical parameters on these electrophysiological features in 2-dimensional heatmaps,  
 518 allowing us to visually determine which parameters were most critical in controlling ISI and  
 519 rebound delay (**Figure 9B, C**):  $g_A$  and  $I_A/I_H V_{50}$  strongly modulated both ISI and rebound delay  
 520 while  $I_A$  tau and  $g_H$  had a weaker influence on these firing properties. To quantify the  
 521 contribution of each biophysical parameter to ISI and rebound delay variations, we then used the  
 522 same strategy already presented in **Figure 8E** for experimental measurements: standardized  
 523 parameters were used to run multiple linear regression against ISI or rebound delay (**Figure 9D**).  
 524 Consistent with the visualization provided in **Figure 9B**, this sensitivity analysis revealed that the  
 525 influence of  $g_A$  and  $I_A/I_H V_{50}$  on ISI and rebound delay was 2-3 times stronger than that of  $g_H$  and  
 526  $I_A$  tau. While the results of this computational modeling are consistent with the general influence  
 527 of  $I_A$  and  $I_H$  reported in these neurons (Liss et al., 2001; Seutin et al., 2001; Neuhoff et al., 2002;  
 528 Puopolo et al., 2007; Amendola et al., 2012; Gantz et al., 2018), they reveal specific effects of  $I_A$   
 529 biophysical properties contrasting with the correlations identified in our experimental data.

530

## 531 **DISCUSSION**

532 The current study provides important elements regarding the identity of the ion channels  
 533 underlying  $I_A$  in SNc DA neurons and the relative influence of specific biophysical parameters of  
 534  $I_A$  (voltage-dependence, gating kinetics, maximal conductance) on neuronal output. In particular,  
 535 in contrast with previous studies (Serodio and Rudy, 1998; Liss et al., 2001; Dufour et al.,  
 536 2014a), we show that the Kv4.2 subunit is expressed in SNc DA neurons, although its functional  
 537 influence appears negligible in most neurons, due to a very low level of expression. In spite of

Kv4.2 presence, we show that the constitutive loss of Kv4.3 is not compensated by complementary intrinsic conductances (Kv4.2-mediated  $I_A$ ,  $I_{KDR}$ ,  $I_H$ ). In addition, while previous studies (Liss et al., 2001; Putzier et al., 2008) and the computational modeling performed here suggest a strong role of  $I_A$  conductance in controlling firing frequency, we demonstrate that  $I_A$  gating kinetics appear as the major determinant of both pacemaking frequency and post-inhibitory rebound delay. Our results also highlight the functional complementarity and correlation of biophysical properties of  $I_A$  and  $I_H$  in these neurons.

#### ***Kv4.2 is expressed in SNc DA neurons***

One of the important results of the present work is the demonstration that Kv4.2 is expressed in mouse SNc DA neurons. So far, it was thought that only Kv4.3 was expressed and entirely responsible for the large A-type current observed in these neurons (Liss and Roeper, 2008; Gantz et al., 2018). Our results however unambiguously demonstrate that Kv4.2 is expressed by SNc DA neurons. First, in the absence of Kv4.1 (Liss et al., 2001; Ding et al., 2011), the presence of an AmmTX3-sensitive residual A-type current in the Kv4.3<sup>-/-</sup> neurons is only compatible with the expression of Kv4.2. While the Kv4.2-mediated residual  $I_A$  is very small and fast in most neurons, in 12% of the voltage clamp-recorded neurons it is large enough to confer a "wild type" phenotype (see **Figure 5, 9**). Even though this residual  $I_A$  current is much faster than its WT counterpart in most neurons, it still influences firing, particularly rebound delay, as suggested by the highly significant correlation between  $I_A$  tau and rebound delay. Second, antigen retrieval immunohistochemistry confirmed that a Kv4.2 staining is observed in a minority (~5%) of SNc DA neurons in both Kv4.3<sup>-/-</sup> and WT mice. While the percentage of cells displaying a "high" expression of Kv4.2 is too small to allow a combined voltage-clamp/AR immunohistochemistry approach, the similarity in the proportion of AmmTX3-sensitive "large residual"  $I_A$  (~12%) and

561 Kv4.2-positive neurons (~5%, not statistically different) strongly suggests that Kv4.2 is  
 562 responsible for a large  $I_A$  in a minority of SNc DA neurons. The presence of a small AmmTX3-  
 563 sensitive residual  $I_A$  in the rest of the Kv4.3<sup>-/-</sup> SNc DA neurons suggests that Kv4.2 is expressed  
 564 and functional in all SNc DA neurons, although its influence might be minor in the presence of  
 565 Kv4.3. The fact that the residual A-type current in Kv4.3<sup>-/-</sup> neurons inactivates faster than its WT  
 566 counterpart is also consistent with the reported differences in inactivation kinetics of Kv4.2 and  
 567 Kv4.3 (Serodio et al., 1994; Serodio et al., 1996). Altogether, these results suggest that, in  
 568 contrast to the widely accepted view, a small subpopulation of SNc DA neurons (~5-10%)  
 569 display an A-type current likely mediated by both Kv4.3 and Kv4.2 channels. Interestingly, these  
 570 two subunits are very similar and co-immunoprecipitate from mouse brain lysates (Marionneau et  
 571 al., 2009), suggesting that they could form heteromeric  $I_A$  channels. At this point however, it is  
 572 difficult to determine whether the Kv4.2-positive neurons in WT mice express Kv4.3/Kv4.2  
 573 heteromers or distinct Kv4.3 and Kv4.2 homomers.

#### 574 ***Lack of homeostatic compensation in Kv4.3<sup>-/-</sup> SNc DA neurons***

575 Intriguingly, these results not only suggest that Kv4.2 expression is very low in most SNc DA  
 576 neurons but also that it is not modified in the Kv4.3<sup>-/-</sup> SNc DA neurons. The structural and  
 577 functional similarities between Kv4.3 and Kv4.2 means that in theory Kv4.2 channels should be  
 578 able to compensate for the loss of Kv4.3. Despite this, the Kv4.2 pattern of expression is not  
 579 modified in Kv4.3<sup>-/-</sup> SNc DA neurons. This is reminiscent of previous studies performed on the  
 580 Kv4.2<sup>-/-</sup> mouse demonstrating that Kv4.3 expression pattern, assessed by western-blot or  
 581 immunohistochemistry, is not modified following Kv4.2 loss (Menegola and Trimmer, 2006;  
 582 Nerbonne et al., 2008). In addition, other currents (such as  $I_{KDR}$  or  $I_H$ ) also appear to not be  
 583 regulated in a compensatory direction in Kv4.3<sup>-/-</sup> SNc DA neurons. The current-clamp

584 comparison between the acute blockade of Kv4 channels in WT neurons and the Kv4.3<sup>-/-</sup> neurons  
 585 also supports this idea of a lack of compensatory modifications in functionally-overlapping  
 586 currents. This is surprising in the light of the results obtained on neonatal cortical pyramidal cells  
 587 (Nerbonne et al., 2008), where Kv4.2 genetic deletion is almost "fully" compensated by an  
 588 increase in sustained potassium currents. To explain this difference, we may hypothesize that,  
 589 although the alteration in electrophysiological phenotype observed in Kv4.3<sup>-/-</sup> neurons is striking  
 590 (see **Figure 3** in particular), the change in calcium dynamics associated with the elevated  
 591 spontaneous activity may not be sufficient to trigger homeostatic regulatory mechanisms  
 592 (O'Leary et al., 2014). Alternatively, modifications in the properties of incoming excitatory or  
 593 inhibitory synaptic inputs (not analyzed in the current study) may compensate for the changes in  
 594 intrinsic activity reported here, such that the overall *in vivo* activity of the SNc network is  
 595 maintained in Kv4.3<sup>-/-</sup> animals. However, behavioral alterations suggest that the change in firing  
 596 of SNc DA neurons is not totally compensated at the network level. Kv4.3<sup>-/-</sup> mice were more  
 597 active than WT littermates in exploring the environment (increased rearing behavior) and could  
 598 not adjust their motor control over sessions on the rotarod. This suggests that the changes in  
 599 midbrain DA neuron tonic firing observed in the Kv4.3<sup>-/-</sup> SNc DA neurons might only be  
 600 revealed when animals are exploring their environment or challenged in a motor learning task.

#### 601 *I<sub>A</sub> gating kinetics play a central role in SNc DA neuron output*

602 The use of I<sub>A</sub> voltage-clamp measurements and current-clamp recordings on a large number of  
 603 neurons in WT and Kv4.3<sup>-/-</sup> mice allowed us to determine the impact of cell-to-cell variations in  
 604 I<sub>A</sub> biophysical properties on spontaneous activity and rebound delay. Interestingly, while realistic  
 605 multi-compartment modeling suggested that I<sub>A</sub> maximal conductance and voltage-dependence  
 606 were the two factors most strongly influencing these electrophysiological features, our recordings

607 revealed that  $I_A$  inactivation rate was the dominant factor defining pacemaking frequency and  
 608 rebound delay (**Figure 9E**).  $I_H$  amplitude (proportional to  $I_H$  maximal conductance in our  
 609 measurements) was also found to play an important role in real neurons, while its influence was  
 610 minor in the model. These differences may be explained by several factors. First, the database  
 611 approach used for our simulations implies that all the tested biophysical properties are varied  
 612 independently (except for the strict correlation applied to  $I_A$  and  $I_H V_{50S}$ ). While the independence  
 613 between these biophysical parameters allowed us to precisely quantify the sensitivity of  
 614 spontaneous activity and rebound delay to each parameter, it does not correspond to the  
 615 observations made in real neurons: for instance  $I_H$  amplitude and  $I_A$  inactivation rate are  
 616 negatively correlated, i.e. not independent from each other. On the other hand, reminiscent of a  
 617 previous study performed on rat neurons (Amendola et al., 2012), we demonstrated that  $I_A$  and  $I_H$   
 618  $V_{50S}$  are also positively correlated in WT mouse neurons. However, this correlation is much  
 619 lower than the one applied in the model ( $r=0.658$ ,  $r^2=0.43$  compared to  $r^2=1$ ) and this difference  
 620 may explain why this biophysical parameter appears as one of the most efficient in modulating  
 621 firing in the model. Thus, the differences in independence of the biophysical properties may  
 622 partly explain why the model and the experimental observations give different answers. Another  
 623 factor may explain why  $I_A$  maximal conductance has a strong effect on firing in the model, but  
 624 not in real neurons. In order to isolate the effect of  $I_A$  and  $I_H$  biophysical properties on firing, all  
 625 other conductances included in the model were held at fixed values. However, every ion current  
 626 displays significant cell-to-cell variations in its properties (gating, conductance density) in a same  
 627 neuronal population (Swensen and Bean, 2005; Schulz et al., 2006; Amendola et al., 2012;  
 628 Moubarak et al., 2019). If happening at random, these variations in other currents would most  
 629 likely dampen the effect of the variations in  $I_A$  or  $I_H$  specific properties on firing. In fact, we  
 630 demonstrated in a previous study (Tapia et al., 2018) that the level of expression of Kv4.3 (at the

mRNA level) in midbrain DA neurons co-varies with the expression levels of multiple somatodendritic ion channels, including Nav1.2, SK3 and GIRK2. If this co-variation is retained at the protein level, it would mean that cell-to-cell variations in  $I_A$  maximal conductance occur in parallel with variations in density of other ion channels. Whether correlated or not, cell-to-cell variations in other conductances may thus explain why  $I_A$  amplitude does not predict pacemaking and rebound delay in real neurons, and why  $I_A$  inactivation rate appears as the main predictor of these electrophysiological features. In contrast with our findings, the results obtained by Liss and colleagues (2001) suggested that Kv4.3 expression level and channel density predicted pacemaking frequency in mouse neurons. Interestingly, it is noteworthy that  $I_A$  inactivation rate showed restricted cell-to-cell variations in their recordings (2-fold range). On the other hand,  $I_A$  charge density showed a 10-fold range of variation, suggesting that most of the variation in  $I_A$  function was due to variations in  $I_A$  maximal conductance (Liss et al., 2001). In our recordings however, the levels of variability observed for  $I_A$  (and  $I_H$ ) biophysical properties were rather similar, which led us to apply a 10-fold range to each parameter in our model. Thus, we postulate that the differences in our conclusions may be essentially related to differences in the cell-to-cell variability range of  $I_A$  and  $I_H$  biophysical parameters recorded in our samples.

#### ***Functional complementarity and co-regulation of $I_A$ and $I_H$ in SNc DA neurons***

While our results confirm the well-established influence of  $I_A$  on SNc DA neuron firing (Liss et al., 2001; Gentet and Williams, 2007; Putzier et al., 2008; Amendola et al., 2012; Tarfa et al., 2017), they also emphasize the functional complementarity between  $I_A$  and  $I_H$  in these neurons, and reinforce the idea that the channels underlying these currents are co-regulated (Amendola et al., 2012). Indeed, we confirm that  $I_A$  and  $I_H$  voltage-dependences are positively correlated and show that  $I_H$  amplitude and  $I_A$  inactivation rate are negatively correlated. While we do not have a



mechanistic explanation for this latter correlation, these results are reminiscent of the observations made by Tarfa and colleagues on nigrostriatal and mesoaccumbal DA neurons (2017). At the functional level, our results demonstrate that these two parameters are the main predictors of the cell-to-cell variations in pacemaking frequency and rebound delay, reinforcing the idea that  $I_A$  and  $I_H$  function as a complementary pair of currents tightly controlling post-inhibitory rebound delay in SNc DA neurons ( $r^2=0.77$ ). The fact that pacemaking rate is not as accurately predicted by  $I_A$  and  $I_H$  properties ( $r^2=0.42$ ) is consistent with the documented role of many other conductances and morphological parameters in defining this firing feature (Nedergaard and Greenfield, 1992; Wilson and Callaway, 2000; Wolfart et al., 2001; Liss et al., 2005; Puopolo et al., 2007; Putzier et al., 2009; Gantz et al., 2018; Moubarak et al., 2019).

## REFERENCES

- Amendola J, Woodhouse A, Martin-Eauclaire MF, Goaillard JM (2012)  $Ca^{2+}$ /cAMP-sensitive covariation of  $I_A$  and  $I_H$  voltage dependences tunes rebound firing in dopaminergic neurons. *J Neurosci* 32:2166-2181.
- Atherton JF, Bevan MD (2005) Ionic Mechanisms Underlying Autonomous Action Potential Generation in the Somata and Dendrites of GABAergic Substantia Nigra Pars Reticulata Neurons In Vitro. *Journal of Neuroscience* 25:8272-8281.
- Bean BP (2007) The action potential in mammalian central neurons. *Nat Rev Neurosci* 8:451-465.
- Benjamini Y, Hochberg Y (1995) Controlling the False Discovery Rate - a Practical and Powerful Approach to Multiple Testing. *J R Stat Soc B* 57:289-300.



- 676 Carrasquillo Y, Burkhalter A, Nerbonne JM (2012) A-type K<sup>+</sup> channels encoded by Kv4.2,  
 677 Kv4.3 and Kv1.4 differentially regulate intrinsic excitability of cortical pyramidal  
 678 neurons. *J Physiol* 590:3877-3890.
- 679 Cembrowski MS, Bachman JL, Wang L, Sugino K, Shields BC, Spruston N (2016) Spatial Gene-  
 680 Expression Gradients Underlie Prominent Heterogeneity of CA1 Pyramidal Neurons.  
 681 *Neuron* 89:351-368.
- 682 Chan CS, Guzman JN, Ilijic E, Mercer JN, Rick C, Tkatch T, Meredith GE, Surmeier DJ (2007)  
 683 'Rejuvenation' protects neurons in mouse models of Parkinson's disease. *Nature* 447:1081-  
 684 1086.
- 685 Destexhe A, Babloyantz A, Sejnowski TJ (1993) Ionic Mechanisms for Intrinsic Slow  
 686 Oscillations in Thalamic Relay Neurons. *Biophysical Journal* 65:1538-1552.
- 687 Ding S, Matta SG, Zhou FM (2011) Kv3-like potassium channels are required for sustained high-  
 688 frequency firing in basal ganglia output neurons. *J Neurophysiol* 105:554-570.
- 689 Dufour MA, Woodhouse A, Goaillard JM (2014a) Somatodendritic ion channel expression in  
 690 substantia nigra pars compacta dopaminergic neurons across postnatal development. *J*  
 691 *Neurosci Res* 92:981-999.
- 692 Dufour MA, Woodhouse A, Amendola J, Goaillard JM (2014b) Non-Linear Developmental  
 693 Trajectory of Electrical Phenotype in Rat Substantia Nigra Pars Compacta Dopaminergic  
 694 Neurons. *eLife* 3:e04059.
- 695 Fuzik J, Zeisel A, Mate Z, Calvigioni D, Yanagawa Y, Szabo G, Linnarsson S, Harkany T (2016)  
 696 Integration of electrophysiological recordings with single-cell RNA-seq data identifies  
 697 neuronal subtypes. *Nat Biotechnol* 34:175-183.

- 698 Gantz SC, Ford CP, Morikawa H, Williams JT (2018) The Evolving Understanding of Dopamine  
 699 Neurons in the Substantia Nigra and Ventral Tegmental Area. *Annu Rev Physiol* 80:219-  
 700 241.
- 701 Gentet LJ, Williams SR (2007) Dopamine gates action potential backpropagation in midbrain  
 702 dopaminergic neurons. *J Neurosci* 27:1892-1901.
- 703 Grace AA, Onn SP (1989) Morphology and electrophysiological properties of  
 704 immunocytochemically identified rat dopamine neurons recorded in vitro. *J Neurosci*  
 705 9:3463-3481.
- 706 Granados-Fuentes D, Norris AJ, Carrasquillo Y, Nerbonne JM, Herzog ED (2012) I(A) channels  
 707 encoded by Kv1.4 and Kv4.2 regulate neuronal firing in the suprachiasmatic nucleus and  
 708 circadian rhythms in locomotor activity. *J Neurosci* 32:10045-10052.
- 709 Guzman JN, Sanchez-Padilla J, Chan CS, Surmeier DJ (2009) Robust pacemaking in substantia  
 710 nigra dopaminergic neurons. *J Neurosci* 29:11011-11019.
- 711 Hines ML, Carnevale NT (2001) NEURON: A tool for neuroscientists. *Neuroscientist* 7:123-135.
- 712 Hodgkin AL, Huxley AF (1952) A quantitative description of membrane current and its  
 713 application to conduction and excitation in nerve. *J Physiol* 117:500-544.
- 714 Hu W, Tian C, Li T, Yang M, Hou H, Shu Y (2009) Distinct contributions of Na(v)1.6 and  
 715 Na(v)1.2 in action potential initiation and backpropagation. *Nat Neurosci* 12:996-1002.
- 716 Ji H, Tucker KR, Putzier I, Huertas MA, Horn JP, Canavier CC, Levitan ES, Shepard PD (2012)  
 717 Functional characterization of ether-a-go-go-related gene potassium channels in midbrain  
 718 dopamine neurons - implications for a role in depolarization block. *Eur J Neurosci*  
 719 36:2906-2916.

- 720 Jiao Y, Sun ZQ, Lee T, Fusco FR, Kimble TD, Meade CA, Cuthbertson S, Reiner A (1999) A  
 721 simple and sensitive antigen retrieval method for free-floating and slide-mounted tissue  
 722 sections. *Journal of Neuroscience Methods* 93:149-162.
- 723 Kole MHP, Stuart GJ (2008) Is action potential threshold lowest in the axon? *Nature*  
 724 *Neuroscience* 11:1253-1255.
- 725 Liss B, Roeper J (2008) Individual dopamine midbrain neurons: functional diversity and  
 726 flexibility in health and disease. *Brain Res Rev* 58:314-321.
- 727 Liss B, Franz O, Sewing S, Bruns R, Neuhoff H, Roeper J (2001) Tuning pacemaker frequency  
 728 of individual dopaminergic neurons by Kv4.3L and KChip3.1 transcription. *EMBO J*  
 729 20:5715-5724.
- 730 Liss B, Haeckel O, Wildmann J, Miki T, Seino S, Roeper J (2005) K-ATP channels promote the  
 731 differential degeneration of dopaminergic midbrain neurons. *Nat Neurosci* 8:1742-1751.
- 732 Lorincz A, Nusser Z (2008) Cell-Type-Dependent Molecular Composition of the Axon Initial  
 733 Segment. *Journal of Neuroscience* 28:14329-14340.
- 734 Marionneau C, LeDuc RD, Rohrs HW, Link AJ, Townsend RR, Nerbonne JM (2009) Proteomic  
 735 analyses of native brain K(V)4.2 channel complexes. *Channels (Austin)* 3:284-294.
- 736 Menegola M, Trimmer JS (2006) Unanticipated region- and cell-specific downregulation of  
 737 individual KChIP auxiliary subunit isoforms in Kv4.2 knock-out mouse brain. *J Neurosci*  
 738 26:12137-12142.
- 739 Moubarak E, Engel D, Dufour MA, Tapia M, Tell F, Goillard JM (2019) Robustness to Axon  
 740 Initial Segment Variation Is Explained by Somatodendritic Excitability in Rat Substantia  
 741 Nigra Dopaminergic Neurons. *Journal of Neuroscience* 39:5044-5063.

- 742 Nedergaard S, Greenfield SA (1992) Subpopulations of Pars Compacta Neurons in the  
 743 Substantia-Nigra - the Significance of Qualitatively and Quantitatively Distinct  
 744 Conductances. *Neuroscience* 48:423-437.
- 745 Nerbonne JM, Gerber BR, Norris A, Burkhalter A (2008) Electrical remodelling maintains firing  
 746 properties in cortical pyramidal neurons lacking KCND2-encoded A-type K<sup>+</sup> currents. *J*  
 747 *Physiol* 586:1565-1579.
- 748 Neuhoﬀ H, Neu A, Liss B, Roeper J (2002) I(h) channels contribute to the different functional  
 749 properties of identified dopaminergic subpopulations in the midbrain. *J Neurosci*  
 750 22:1290-1302.
- 751 Niwa N, Wang W, Sha Q, Marionneau C, Nerbonne JM (2008) Kv4.3 is not required for the  
 752 generation of functional I<sub>to</sub> channels in adult mouse ventricles. *J Mol Cell Cardiol*  
 753 44:95-104.
- 754 Northcutt AJ, Kick DR, Otopalik AG, Goetz BM, Harris RM, Santin JM, Hofmann HA, Marder  
 755 E, Schulz DJ (2019) Molecular proﬁling of single neurons of known identity in two  
 756 ganglia from the crab *Cancer borealis*. *P Natl Acad Sci USA* 116:26980-26990.
- 757 O'Leary T, Williams AH, Franci A, Marder E (2014) Cell types, network homeostasis, and  
 758 pathological compensation from a biologically plausible ion channel expression model.  
 759 *Neuron* 82:809-821.
- 760 Philippart F, Destreel G, Merino-Sepulveda P, Henny P, Engel D, Seutin V (2016) Differential  
 761 Somatic Ca<sup>2+</sup> Channel Profile in Midbrain Dopaminergic Neurons. *J Neurosci* 36:7234-  
 762 7245.
- 763 Puopolo M, Raviola E, Bean BP (2007) Roles of subthreshold calcium current and sodium  
 764 current in spontaneous firing of mouse midbrain dopamine neurons. *J Neurosci* 27:645-  
 765 656.

- 766 Putzier I, Kullmann PHM, Horn JP, Levitan ES (2008) Dopamine Neuron Responses Depend  
767 Exponentially on Pacemaker Interval. *Journal of Neurophysiology* 101:926-933.
- 768 Putzier I, Kullmann PHM, Horn JP, Levitan ES (2009) Cav1.3 Channel Voltage Dependence,  
769 Not  $\text{Ca}^{2+}$  Selectivity, Drives Pacemaker Activity and Amplifies Bursts in Nigral  
770 Dopamine Neurons. *Journal of Neuroscience* 29:15414-15419.
- 771 Schulz DJ, Goaillard JM, Marder E (2006) Variable channel expression in identified single and  
772 electrically coupled neurons in different animals. *Nat Neurosci* 9:356-362.
- 773 Serodio P, Rudy B (1998) Differential expression of Kv4  $\text{K}^{+}$  channel subunits mediating  
774 subthreshold transient  $\text{K}^{+}$  (A-type) currents in rat brain. *J Neurophysiol* 79:1081-1091.
- 775 Serodio P, Kentros C, Rudy B (1994) Identification of Molecular-Components of a-Type  
776 Channels Activating at Subthreshold Potentials. *Journal of Neurophysiology* 72:1516-  
777 1529.
- 778 Serodio P, Vega-Saenz de Miera E, Rudy B (1996) Cloning of a novel component of A-type  $\text{K}^{+}$   
779 channels operating at subthreshold potentials with unique expression in heart and brain.  
780 *Journal of Neurophysiology* 75:2174-2179.
- 781 Seutin V, Engel D (2010) Differences in  $\text{Na}^{+}$  conductance density and  $\text{Na}^{+}$  channel functional  
782 properties between dopamine and GABA neurons of the rat substantia nigra. *J*  
783 *Neurophysiol* 103:3099-3114.
- 784 Seutin V, Massotte L, Renette MF, Dresse A (2001) Evidence for a modulatory role of  $I_h$  on the  
785 firing of a subgroup of midbrain dopamine neurons. *Neuroreport* 12:255-258.
- 786 Swensen AM, Bean BP (2005) Robustness of burst firing in dissociated purkinje neurons with  
787 acute or long-term reductions in sodium conductance. *J Neurosci* 25:3509-3520.
- 788 Tapia M, Baudot P, Formisano-Treziny C, Dufour MA, Temporal S, Lasserre M, Marqueze-  
789 Pouey B, Gabert J, Kobayashi K, Goaillard JM (2018) Neurotransmitter identity and

790 electrophysiological phenotype are genetically coupled in midbrain dopaminergic  
791 neurons. *Sci Rep* 8:13637.

792 Tarfa RA, Evans RC, Khaliq ZM (2017) Enhanced Sensitivity to Hyperpolarizing Inhibition in  
793 Mesoaccumbal Relative to Nigrostriatal Dopamine Neuron Subpopulations. *Journal of*  
794 *Neuroscience* 37:3311-3330.

795 Taylor AL, Hickey TJ, Prinz AA, Marder E (2006) Structure and visualization of high-  
796 dimensional conductance spaces. *J Neurophysiol* 96:891-905.

797 Vacher H, Alami M, Crest M, Possani LD, Bougis PE, Martin-Eauclaire MF (2002) Expanding  
798 the scorpion toxin alpha-KTX 15 family with AmmTX3 from *Androctonus mauretanicus*.  
799 *Eur J Biochem* 269:6037-6041.

800 Wilson CJ, Callaway JC (2000) Coupled oscillator model of the dopaminergic neuron of the  
801 substantia nigra. *J Neurophysiol* 83:3084-3100.

802 Wolfart J, Neuhoﬀ H, Franz O, Roeper J (2001) Differential expression of the small-  
803 conductance, calcium-activated potassium channel SK3 is critical for pacemaker control  
804 in dopaminergic midbrain neurons. *J Neurosci* 21:3443-3456.

805

## 806 FIGURE LEGENDS

807 **Figure 1. Behavioral assessment of the  $Kv4.3^{-/-}$  transgenic mouse.** A, locomotion measured in  
808 actimetry chambers. Left, line and scatter plot showing the mean number of horizontal  
809 movements per 5-min bin ( $\pm$  SEM) in  $Kv4.3^{-/-}$  mice (red) compared to their WT littermates  
810 (black). Right, line and scatter plot showing the mean number of rearing events per 5-min bin in  
811  $Kv4.3^{-/-}$  mice (red) compared to their WT littermates (black). Significant differences between

812 strains for specific time bins (two-way repeated measures ANOVA) are indicated by an asterisk.  
813 **B**, changes in motor learning measured using a rotarod assay. The latency to falling off the  
814 rotating rod (with increasing rotating speed) was assessed over 10 consecutive trials (left).  
815 Significant differences between strains for specific trials (two-way repeated measures ANOVA)  
816 are indicated by an asterisk. The performance index ((average latency 8-10)/(average latency 1-  
817 3)\*100, right) was used to evaluate the learning ability of Kv4.3<sup>-/-</sup> mice (red) compared to their  
818 WT littermates (black). \* p<0.05, \*\* p<0.01.

819

820 **Figure 2. Spontaneous activity and post-inhibitory rebound are profoundly altered in**  
821 **Kv4.3<sup>-/-</sup> SNc DA neurons.** **A**, representative cell-attached recordings showing the spontaneous  
822 pattern of activity in WT (black trace, left) and Kv4.3<sup>-/-</sup> SNc DA neurons (red trace, right). **B**, box  
823 and whisker plots showing the distribution of values for extracellularly recorded spontaneous ISI  
824 (Extracellular ISI, left) and ISI coefficient of variation (CV<sub>extra. ISI</sub>, right) in WT and Kv4.3<sup>-/-</sup> SNc  
825 DA neurons. **C**, representative current-clamp recordings showing the voltage response of SNc  
826 DA neurons to a current step (gray trace) hyperpolarizing membrane voltage to ~ -120mV in WT  
827 (black trace, left) and Kv4.3<sup>-/-</sup> mice (red trace, right). The recordings come from the same  
828 neurons as the cell-attached recordings presented in **A**. **D**, box and whisker plots showing the  
829 distribution of values for voltage sag amplitude (left) and post-inhibitory rebound delay (right) in  
830 WT and Kv4.3<sup>-/-</sup> SNc DA neurons. \*\*\* p<0.001. Dotted lines in the box and whisker plots  
831 indicate the distribution of data (violin plots). Scale bars: **A**, horizontal 1s; **C**, top, horizontal  
832 500ms, vertical 40mV; bottom, vertical 100pA; horizontal dotted lines indicate -60mV.

833

**Figure 3. Action potential and excitability properties in Kv4.3<sup>-/-</sup> SNc DA neurons.** **A**, left, current-clamp recordings showing the shape of the action potential in the WT (black traces) and Kv4.3<sup>-/-</sup> mice (red traces) on a slow (top) and fast time-scale (bottom). Right, box and whisker plots showing the distribution of values for action potential threshold (top left), amplitude (top right), half-width (AP half-width, bottom left) and afterhyperpolarization trough (AHP trough, bottom right) in WT and Kv4.3<sup>-/-</sup> SNc DA neurons. **B**, left, current-clamp recordings showing the voltage response of SNc DA neurons to 100 and 200pA depolarizing current steps (gray traces) in WT (top, black traces) and Kv4.3<sup>-/-</sup> mice (bottom, red traces). Gray dotted rectangles indicate the interspike interval used to calculate the gain start and gain end on each train of action potentials. Right, box and whisker plots showing the distribution of values for gain start (top left), gain end (top right), spike frequency adaptation (SFA) index (bottom left) and start frequency at 100pA (bottom right) in WT and Kv4.3<sup>-/-</sup> SNc DA neurons. \* p<0.05, \*\* p<0.01, \*\*\* p<0.001. Dotted lines in the box and whisker plots indicate the distribution of data (violin plots). Scale bars: **A**, top, horizontal 50ms, vertical 20mV; **A**, bottom, horizontal 2ms, vertical 20mV, horizontal dotted lines indicate -40mV; **B**, voltage, horizontal 500ms, vertical 40mV; current, vertical 100pA.

**Figure 4. Voltage-clamp analysis of I<sub>A</sub> in wild-type and Kv4.3<sup>-/-</sup> SNc DA neurons.** **A**, voltage-clamp traces showing representative I<sub>A</sub> recordings obtained from a WT (black trace) and a Kv4.3<sup>-/-</sup> SNc DA neuron (red trace) in response to a voltage step to -40mV (gray trace). The small residual current present in the Kv4.3<sup>-/-</sup> mice is blocked by AmmTX3 (inset, orange trace). **B**, box and whisker plot showing the distribution of values for I<sub>A</sub> amplitude in WT and Kv4.3<sup>-/-</sup> SNc DA neurons. **C**, box and whisker plot showing the distribution of values for I<sub>A</sub> time constant of



857 inactivation ( $I_A$  tau) in WT and Kv4.3<sup>-/-</sup> SNc DA neurons. The green dotted rectangle highlights 5  
858 Kv4.3<sup>-/-</sup> outliers displaying unusually large values for  $I_A$  tau. **D**, box and whisker plot showing the  
859 distribution of values for  $I_A$  charge in WT and Kv4.3<sup>-/-</sup> SNc DA neurons. The green dotted  
860 rectangle highlights 5 Kv4.3<sup>-/-</sup> outliers displaying unusually large values for  $I_A$  charge (same cells  
861 as in **C**). **E**, left, scatter plot showing the relationship between  $I_A$  tau and charge in WT (gray  
862 dots) and Kv4.3<sup>-/-</sup> SNc DA neurons (red dots). Please note that 5 of the Kv4.3<sup>-/-</sup> measurements lie  
863 in the WT region of space (green dotted ellipse). Right, voltage-clamp traces showing one  
864 example of the atypical  $I_A$  recording (green trace, corresponding to the large green circle in the  
865 scatter plot) encountered in one of the 5 Kv4.3<sup>-/-</sup> outliers highlighted in panels **C** and **D**,  
866 compared to the typical recording obtained in Kv4.3<sup>-/-</sup> neurons (red trace, same as in panel **A**,  
867 corresponding to the large red circle in the scatter plot). \*\*\*  $p < 0.001$ . Dotted lines in the box and  
868 whisker plots indicate the distribution of data (violin plots). Scale bars in **A** and **E**: horizontal  
869 200ms, vertical 1nA.

870

871 **Figure 5. Kv4.2 channels are expressed by a minority of wild-type and Kv4.3<sup>-/-</sup> SNc DA**  
872 **neurons.** **A**, Top, low-magnification pictures of the SNc showing (from left to right) TH (red),  
873 Kv4.3 (green) and DAPI (blue) stainings in WT (top row) and Kv4.3<sup>-/-</sup> mice (bottom row).  
874 Bottom, high-magnification pictures of SNc DA neurons showing (from left to right) TH (red),  
875 Kv4.3 (green) and DAPI (blue) stainings in WT (top row) and Kv4.3<sup>-/-</sup> mice (bottom row). **B**,  
876 effect of the antigen retrieval procedure on Kv4.2 detection in the SNc. Top, low-magnification  
877 pictures showing (from left to right) TH (red), Kv4.2 (green) and DAPI staining (blue) without  
878 (top row) or with antigen retrieval (bottom row). Bottom, left, high-magnification pictures of the  
879 insets depicted in the merged low-magnification picture and corresponding to a Kv4.2-negative

880 (left) and a Kv4.2-positive SNc DA neuron (middle), for which inset pictures (right) illustrate the  
 881 region selected to characterize the immunofluorescence profile of Kv4.2 and TH stainings (3µm  
 882 yellow bar). Bottom, right, immunofluorescence profiles of Kv4.2 (green, top graph), Kv4.3  
 883 (green, bottom graph) and TH staining (red, both graphs), showing that both Kv4.2 and Kv4.3  
 884 profiles are very similar and strongly suggestive of specific plasma membrane expression. The  
 885 average profiles (n=5) shown here were defined over 3µm selected regions of (yellow bar above  
 886 the graph), such as the one shown on the inset pictures on the left. **C**, left, high-magnification  
 887 pictures showing (from left to right) TH (red), Kv4.2 (green) and DAPI staining (blue) after  
 888 antigen retrieval in WT (top row) and Kv4.3<sup>-/-</sup> mice (bottom row). Right, expanded view of the  
 889 Kv4.2-positive cells (1, 2) highlighted in the merged pictures on the left. **D**, bar plot showing the  
 890 counts of Kv4.2-negative (dark colors) and -positive (light colors) cells observed in the SNc of  
 891 WT (black bar) and Kv4.3<sup>-/-</sup> mice (red bar). n.s. non-significant. Scale bars: **A**, top row 100µm,  
 892 bottom row 10µm; **B**, top row 10µm, bottom row 10µm, inset 2µm; **C**, 10µm.

893

894 **Figure 5-1. Validation of antigen retrieval Kv4.2 immunohistochemistry on neocortical and**  
 895 **hippocampal neurons.** **A**, low-magnification (top rows) and high-magnification pictures  
 896 (bottom rows) showing the effect of the antigen retrieval procedure on Kv4.2 immunostaining  
 897 (green) in the cortex. DAPI staining (blue) is also shown. **B**, low-magnification (top rows) and  
 898 high-magnification pictures (bottom rows) showing the effect of the antigen retrieval procedure  
 899 on Kv4.2 immunostaining (green) in the CA1 region of the hippocampus. DAPI staining (blue) is  
 900 also shown. **A**, top row 100µm, bottom row 10µm; **B**, top row 100µm, bottom row 10µm.

901

902

903 **Figure 6. Comparing the alterations in electrophysiological phenotype after acute blockade**  
 904 **of Kv4 channels with the Kv4.3<sup>-/-</sup> mouse model.** **A**, current-clamp recordings showing the  
 905 spontaneous pattern of activity of a WT SNc DA neuron in control condition (black trace, left)  
 906 and after AmmTX3 application (red trace, right). **B**, left, line and scatter plot showing the change  
 907 in spontaneous firing frequency induced by AmmTX3 application in individual WT SNc DA  
 908 neurons. Right, bar plot comparing the average change in spontaneous firing frequency after  
 909 AmmTX3 application (left, light colors) or Kv4.3 channel deletion (right, dark colors). **C**,  
 910 current-clamp recordings showing the voltage response of a WT SNc DA neuron to a  
 911 hyperpolarizing current step (bottom gray traces) in control condition (left, black trace) and after  
 912 AmmTX3 application (right, red trace). **D**, left, line and scatter plot showing the change in  
 913 rebound delay induced by AmmTX3 application in individual WT SNc DA neurons. Right, bar  
 914 plot showing the average change in rebound delay after AmmTX3 application (left, light colors)  
 915 or Kv4.3 channel deletion (right, dark colors). \*\* p<0.01, \*\*\* p<0.001. Scale bars: **A**, horizontal  
 916 1s, vertical 20mV, horizontal gray dotted lines indicate -60mV; **C**, horizontal 500ms, vertical  
 917 20mV.

918

919 **Figure 7. Absence of compensatory changes in delayed rectifier and I<sub>H</sub> currents in the**  
 920 **Kv4.3<sup>-/-</sup> SNc DA neurons.** **A**, properties of the delayed rectifier potassium current (I<sub>KDR</sub>) in SNc  
 921 DA neurons in WT and Kv4.3<sup>-/-</sup> mice. Left, voltage-clamp recordings of I<sub>KDR</sub> obtained in a WT  
 922 (black trace) and a Kv4.3<sup>-/-</sup> mouse (red trace) in response to a voltage step to +20mV (gray trace).  
 923 The peak and steady-state components of I<sub>KDR</sub> are indicated by arrowheads. Right, line and

924 scatter plots representing the average current-voltage relationships of the peak (left) and steady-  
 925 state  $I_{KDR}$  (right) obtained from WT (gray dots) and  $Kv4.3^{-/-}$  SNc DA neurons (red dots). **B**,  
 926 properties of  $I_H$  in SNc DA neurons in WT and  $Kv4.3^{-/-}$  mice. Left, voltage-clamp recordings of  
 927  $I_H$  obtained in a WT (black traces) and a  $Kv4.3^{-/-}$  mouse (red traces) in response to increasingly  
 928 hyperpolarized voltage steps. Right, box and whisker plot showing the distribution of values for  
 929  $I_H$  amplitude (left) and voltage sensitivity (right) in WT and  $Kv4.3^{-/-}$  SNc DA neurons. \*\*\*  
 930  $p < 0.001$ . Dotted lines in the box and whisker plots indicate the distribution of data (violin plots).  
 931 Scale bars: **A**, horizontal 200ms, vertical 1nA; **B**, horizontal 2s, vertical 500pA.

932  
 933 **Figure 8. Linking biophysical changes in  $I_A$  to changes in electrophysiological phenotype in**  
 934 **wild-type and  $Kv4.3^{-/-}$  SNc DA neurons.** **A**, recordings representative of the variation in  
 935 spontaneous activity, post-inhibitory rebound and  $I_A$  in WT and  $Kv4.3^{-/-}$  SNc DA neurons. Left,  
 936 cell-attached voltage-clamp recordings of spontaneous pacemaking activity in 2 WT (black  
 937 traces) and 2  $Kv4.3^{-/-}$  neurons (red traces). The value of the average ISI is indicated above the  
 938 trace. Middle, current-clamp recordings of the post-inhibitory rebound obtained in the same  
 939 neurons. The value of rebound delay is indicated above the trace. Right,  $I_A$  voltage-clamp  
 940 recordings obtained at -40mV in the same neurons. The values of  $I_A$  amplitude and tau are  
 941 indicated above the trace. **B**, scatter plot showing the significant positive correlation between  
 942 extracellularly recorded ISI and rebound delay observed in WT (gray dots) and  $Kv4.3^{-/-}$  SNc DA  
 943 neurons (red dots). The plain black and red lines correspond to the linear regression of the data ( $r$ ,  
 944  $n$  and  $p$  values are shown on the graph), while the gray and pink dotted lines indicate the  
 945 regression confidence intervals. The diamond and square symbols correspond to the recordings  
 946 presented in panel A. **C**, scatter plots showing the relationships between biophysical variables

947 and neuronal output. Correlations between  $I_A$  tau,  $I_H$  amplitude,  $I_A$  amplitude or  $I_A V_{50}$  (from left  
 948 to right) and rebound delay or extracellular ISI (from top to bottom) were tested in both WT (gray  
 949 dots) and  $Kv4.3^{-/-}$  neurons (red dots). Please note that only  $I_A$  tau and  $I_H$  amplitude were  
 950 significantly correlated with both ISI and rebound delay in WT and  $Kv4.3^{-/-}$  neurons. The plain  
 951 black and red lines correspond to the linear regression of the data ( $r/\rho$ ,  $n$  and  $p$  values are shown  
 952 on the graph), while the gray and pink dotted lines indicate the regression confidence intervals.  
 953 Dashed black and red lines indicate non-significant correlations. The diamond and square  
 954 symbols correspond to the recordings presented in panel **A**. **D**, scatter plots showing the  
 955 significant correlations between  $I_A$  and  $I_H$  properties. Left, scatter plot showing the positive  
 956 correlation between  $I_A$  inactivation  $V_{50}$  and  $I_H$  activation  $V_{50}$  in WT neurons. Right, scatter plot  
 957 showing the negative correlation between  $I_A$  tau and  $I_H$  amplitude observed in both WT (gray  
 958 dots) and  $Kv4.3^{-/-}$  neurons (red dots). The plain black and red lines correspond to the linear  
 959 regression of the data ( $r/\rho$ ,  $n$  and  $p$  values are shown on the graph), while the gray and pink  
 960 dotted lines indicate the regression confidence intervals. **E**, left, scatter plot showing the multiple  
 961 linear regression of extracellular ISI vs  $I_A$  tau and  $I_H$  amplitude (predicted ISI) in WT neurons.  
 962 Right, scatter plot showing the multiple linear regression of rebound delay vs  $I_A$  tau,  $I_A$   
 963 inactivation  $V_{50}$  and  $I_H$  amplitude (predicted rebound delay) in WT neurons. The corresponding  
 964 equations are indicated below the X axis of each graph. The plain black lines correspond to the  
 965 linear regression of the data ( $r$ ,  $n$  and  $p$  values are shown on the graph), while the gray dotted  
 966 lines indicate the regression confidence intervals. Scale bars: **A**, left horizontal 1s; middle  
 967 horizontal 500ms, vertical 50mV; right horizontal 250ms, vertical 2nA.

968

969 **Figure 9. Modeling the effect of the biophysical properties of  $I_A$  and  $I_H$  on spontaneous**  
 970 **activity and post-inhibitory rebound.** **A**, table presenting the 5 values tested for each  
 971 biophysical parameter ( $g_A$ ,  $g_H$ ,  $I_A/I_H$ ,  $V_{50}$  and  $I_A$  inactivation tau) in the multi-compartment model.  
 972 Each property was varied independently, leading to 625 ( $5^4$ ) versions of the model. **B**,  
 973 dimensionally stacked heatmaps showing the variation in ISI (displayed as  $\log(\text{ISI})$ , left) and in  
 974 post-inhibitory rebound delay (displayed as  $\log(\text{rebound delay})$ , right) as a function of  $g_A$  (X axis,  
 975 big scale),  $I_A/I_H$   $V_{50}$  (Y axis, big scale),  $I_A$  tau (X axis, small scale) and  $g_H$  (Y axis, small scale).  
 976 **C**, example traces of spontaneous pacemaking (left) and post-inhibitory rebound (right) obtained  
 977 for the minimal and maximal values of  $g_A$  and  $I_A$  tau (corresponding to the 4 squares surrounded  
 978 in the panel **B** heatmaps). The gray horizontal bars above the traces help visualize the change in  
 979 ISI (left) or rebound delay (right) as a function of changes in  $g_A$  and  $I_A$  tau. **D**, multiple linear  
 980 regression reveals the relative contribution of each biophysical property to ISI (left) or rebound  
 981 delay variation (right). The scatter plots show the relationship between the measured values of  
 982  $\log(\text{ISI})$  and  $\log(\text{rebound delay})$  and the values predicted using a linear combination of the 4  
 983 biophysical variables listed in panel **A** (the corresponding equations are shown above each  
 984 graph). Scale bars: **C**, horizontal 500ms, vertical 50mV.

985  
 986 **Table 1. Statistical analysis of electrophysiological parameters in wild-type and  $Kv4.3^{-/-}$  SNc**  
 987 **DA neurons.** The values for 16 electrophysiological parameters measured under current-clamp  
 988 (corresponding to passive properties, spontaneous activity, post-inhibitory rebound, action  
 989 potential and excitability) and 8 electrophysiological parameters measured under voltage-clamp  
 990 (corresponding to  $I_A$  and  $I_H$  properties) are presented for WT and  $Kv4.3^{-/-}$  SNc DA neurons. Mean  
 991 and SD (black text) are reported for normally-distributed data, while Median and interquartile

992 range (IQR) are reported otherwise (gray text). Accordingly, statistical differences between WT  
993 and Kv4.3<sup>-/-</sup> neurons were tested using a t-test or a Mann Whitney test, depending on the  
994 normality of the data. Asterisks indicate statistically significant differences (\* p<0.05, \*\* p<0.01,  
995 \*\*\* p<0.001).

996

997 **Table 2. Equations governing the voltage dependence and kinetics of currents in the model**

998

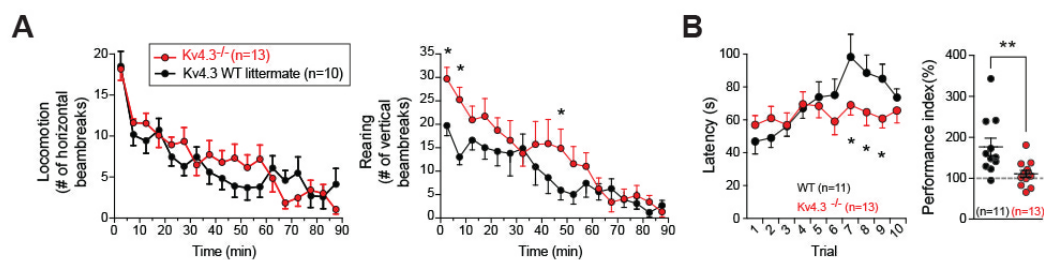


FIGURE 1



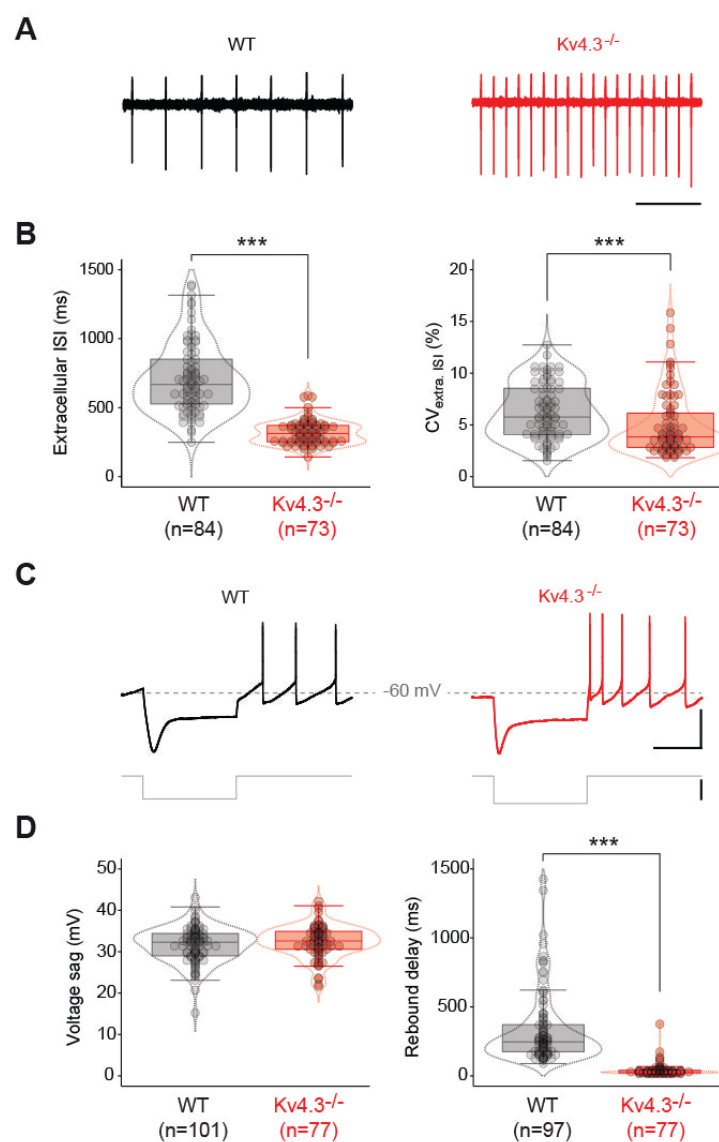


FIGURE 2

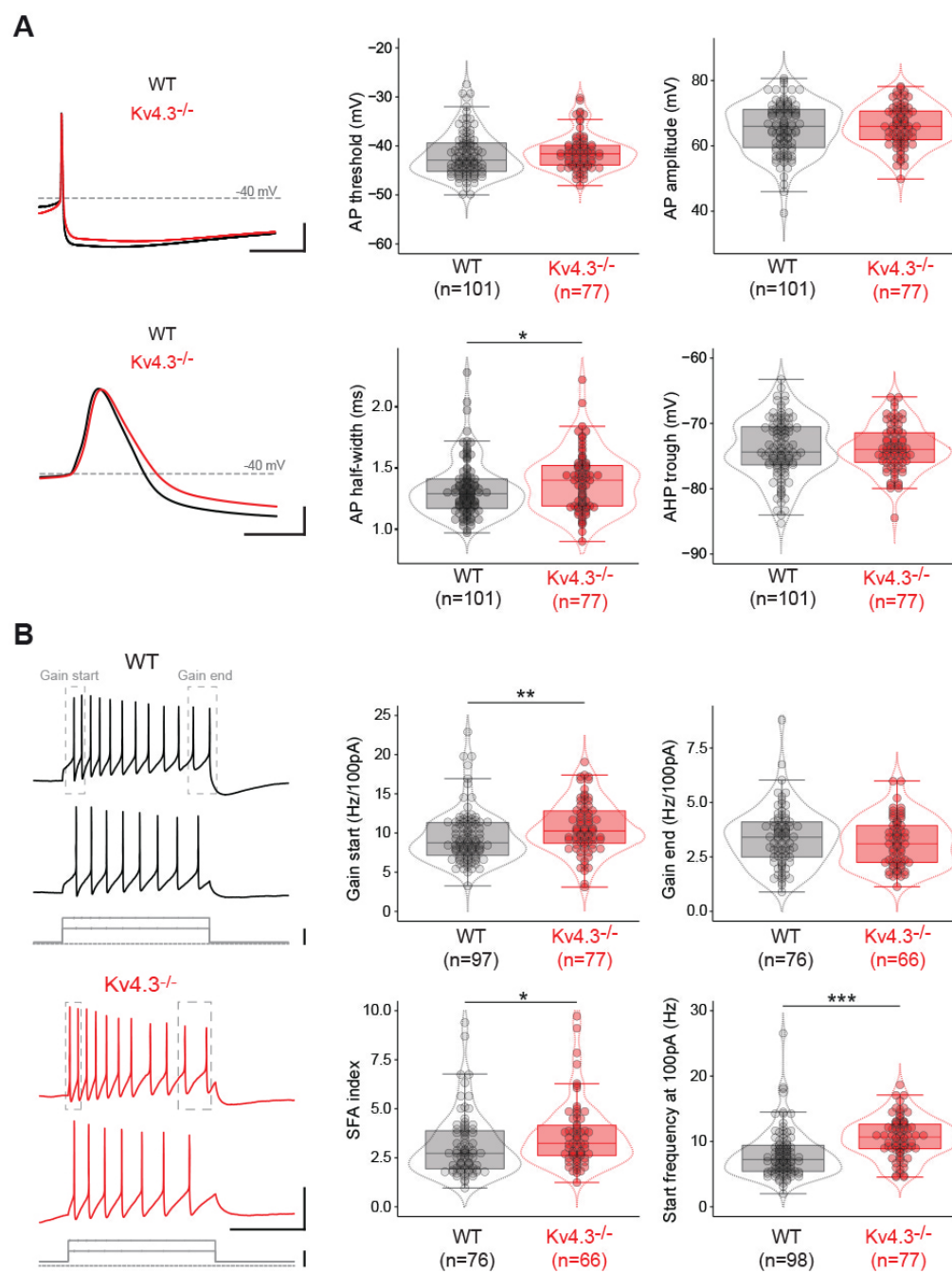


FIGURE 3

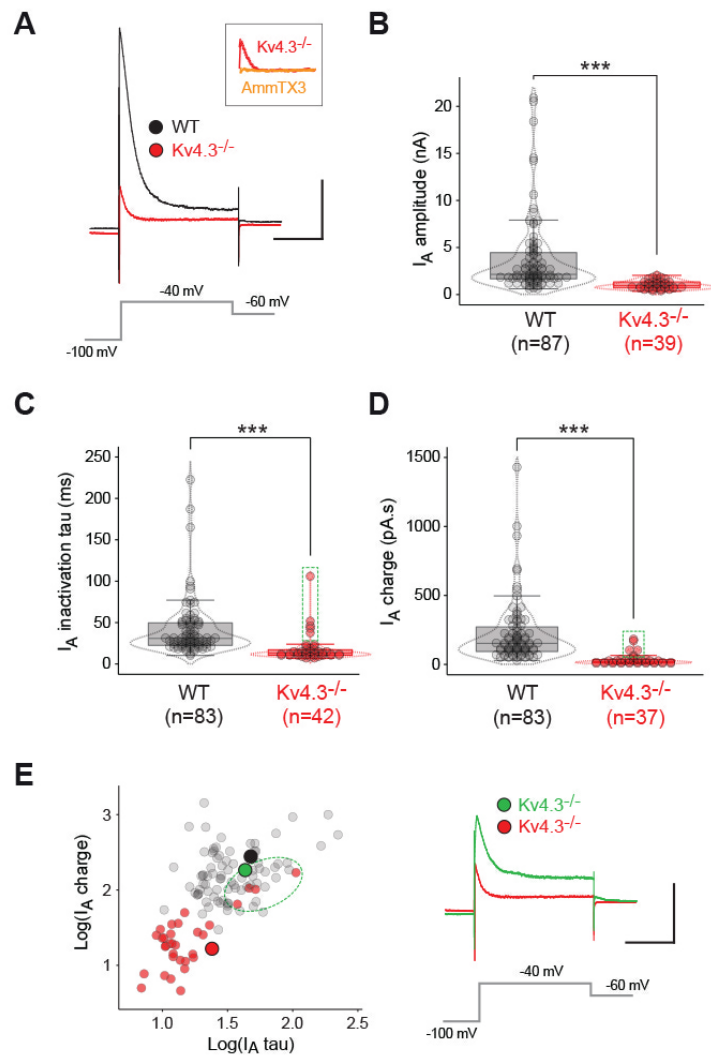


FIGURE 4

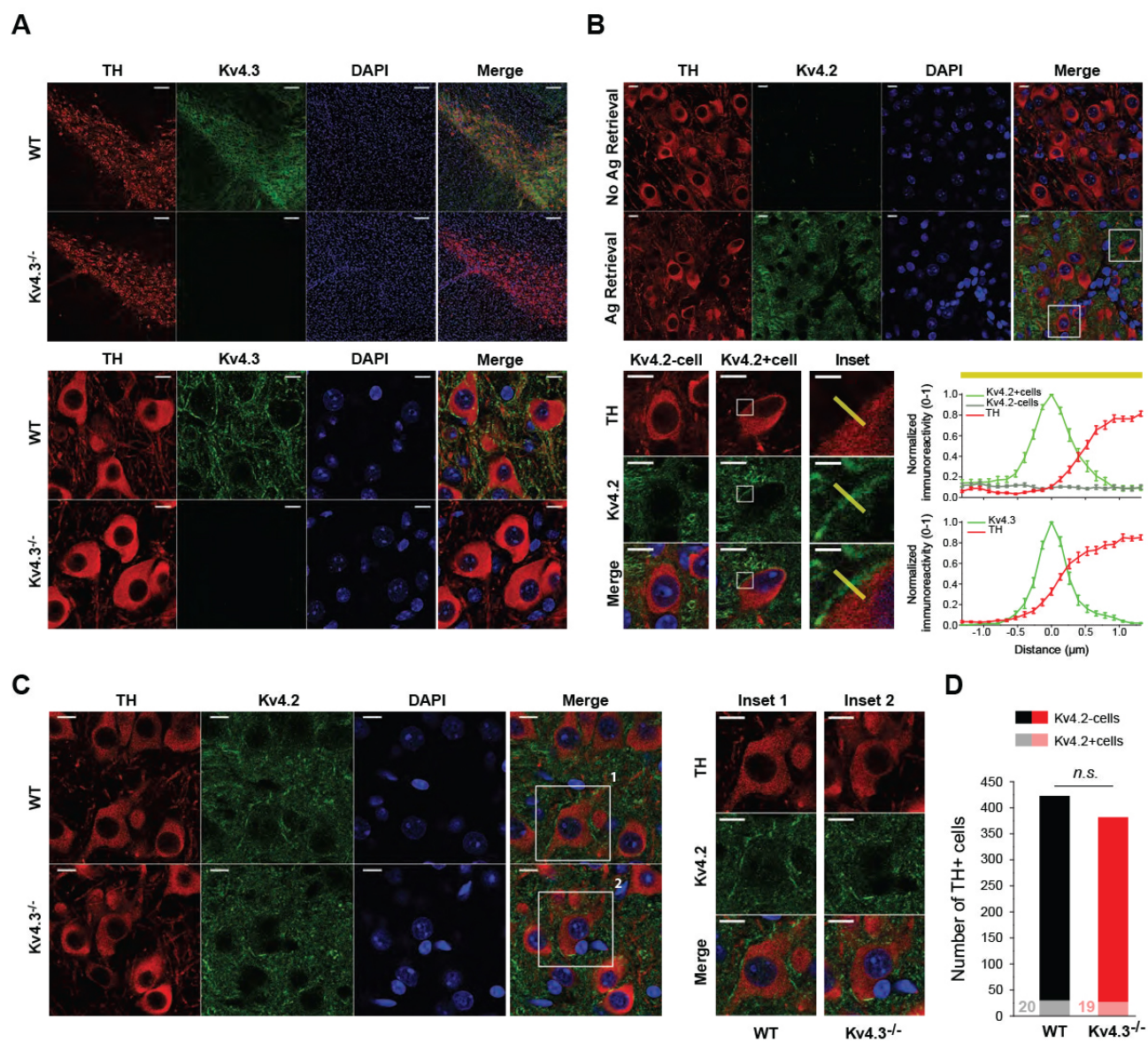


FIGURE 5

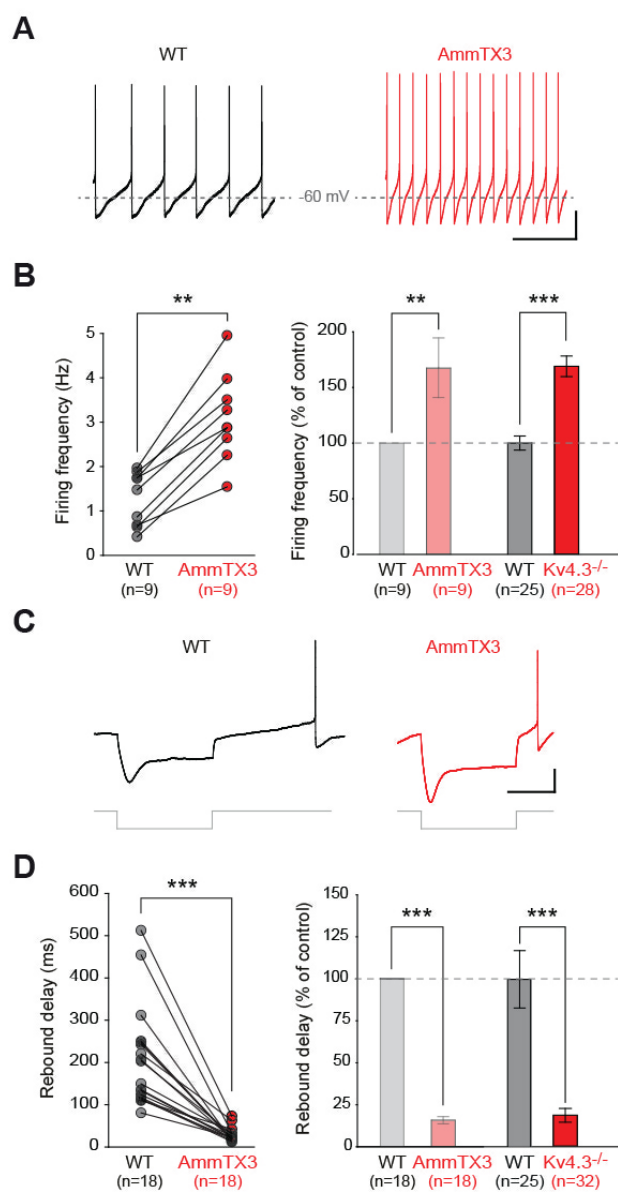


FIGURE 6

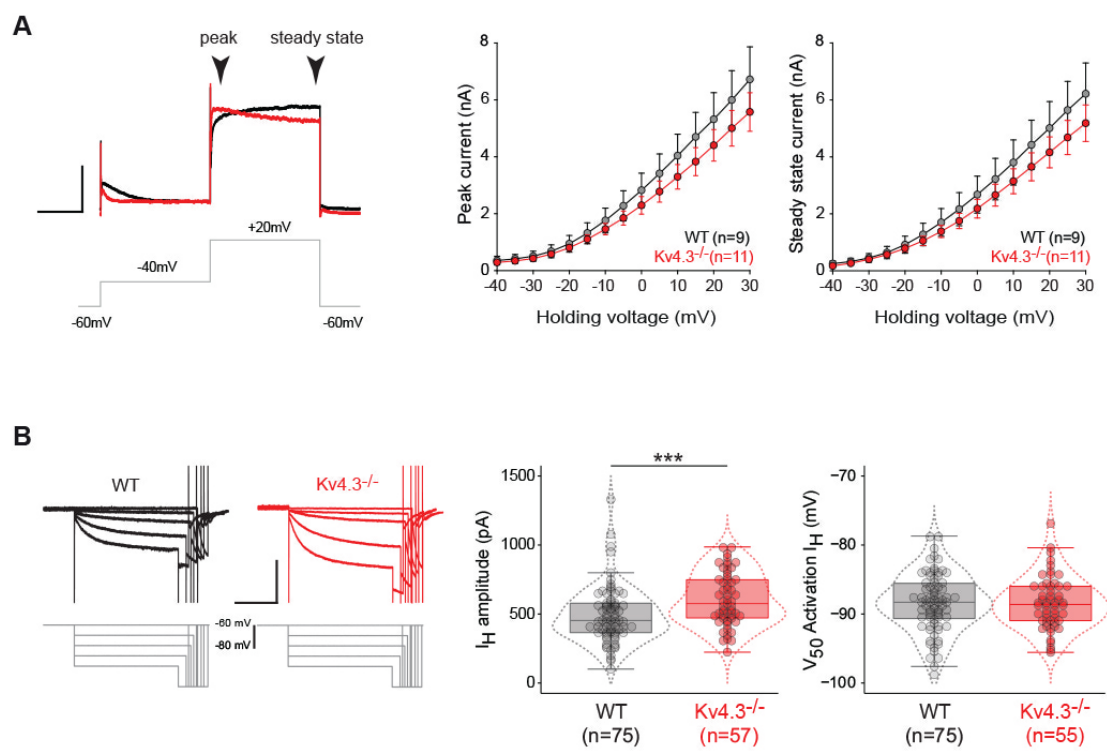


FIGURE 7



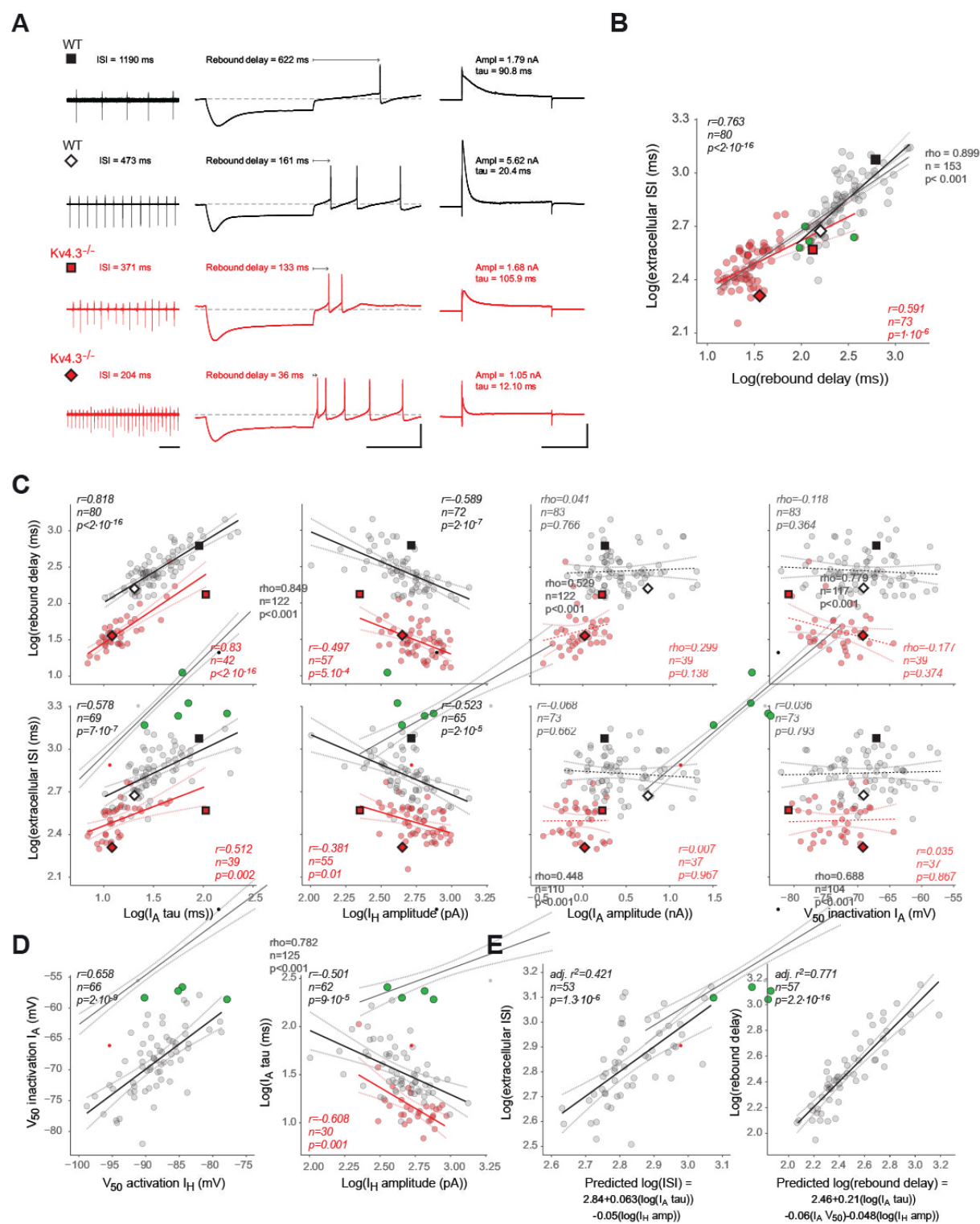


FIGURE 8

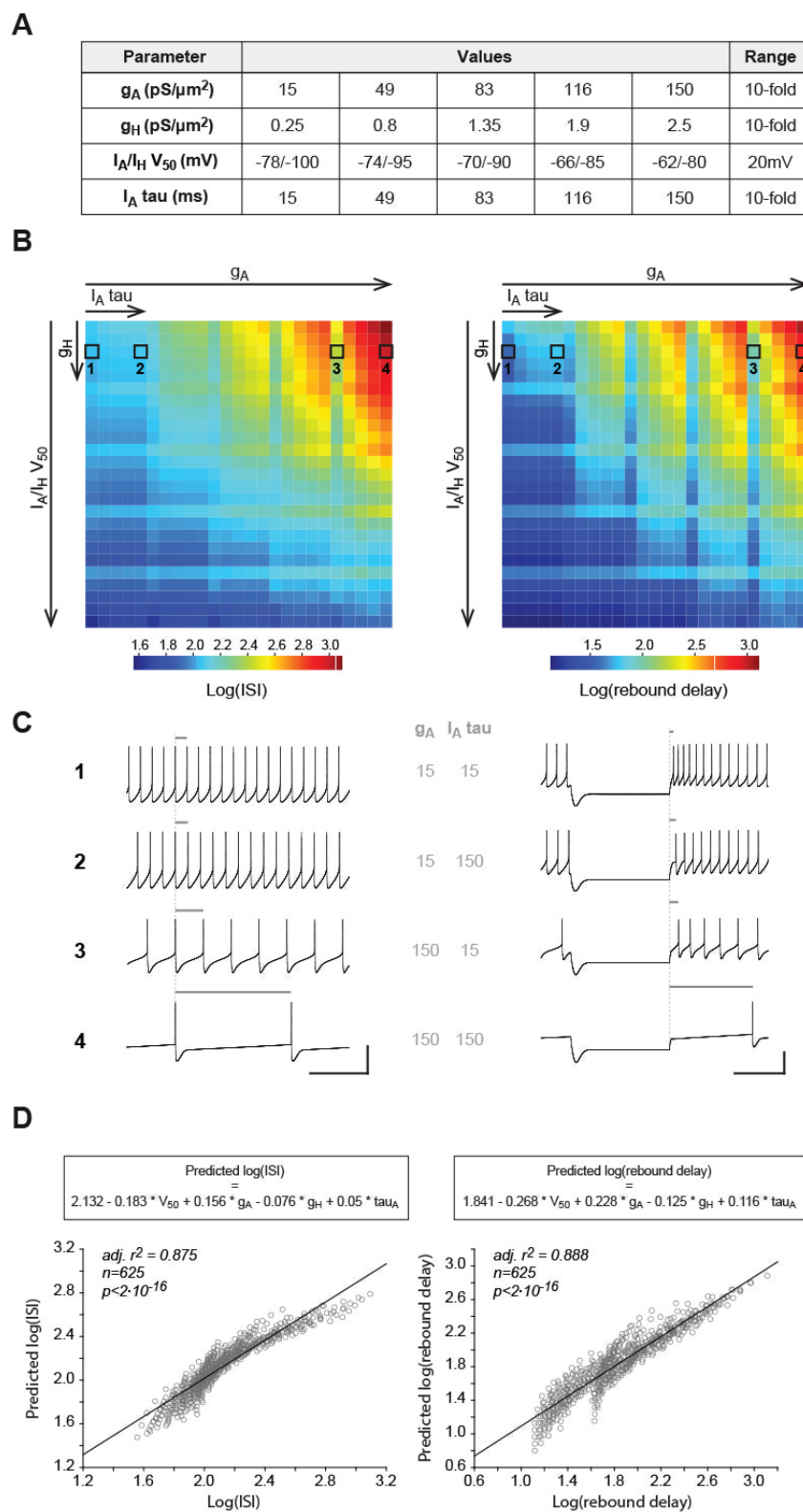


FIGURE 9